DEVELOPING WAVELET-BASED POST-PROCESSING TECHNIQUES FOR SOLID-STATE QUANTUM SENSING APPLICATIONS

A DISSERTATION SUBMITTED TO

THE GRADUATE SCHOOL OF ENGINEERING AND SCIENCE

OF BILKENT UNIVERSITY

IN PARTIAL FULFILLMENT OF THE REQUIREMENTS FOR

THE DEGREE OF

DOCTOR OF PHILOSOPHY

IN

PHYSICS

By

Ekrem Taha Güldeste

August 2024

Developing wavelet-based post-processing techniques for solid-state quantum sensing applications
By Ekrem Taha Güldeste
August 2024

We certify that we have read this dissertation and that in our opinion it is fully adequate, in scope and in quality, as a dissertation for the degree of Doctor of Philosophy.

Ceyhun Bulutay(Advisor)

Mehmet Özgür Oktel

Ahmet Keleş

Deniz Aybaş Tümtürk

Mehmet Emre Taşgın

Approved for the Graduate School of Engineering and Science:

Orhan Arıkan
Director of the Graduate School

ABSTRACT

DEVELOPING WAVELET-BASED POST-PROCESSING TECHNIQUES FOR SOLID-STATE QUANTUM SENSING APPLICATIONS

Ekrem Taha Güldeste
Ph.D. in Physics
Advisor: Ceyhun Bulutay
August 2024

Spin manifolds of defect centers formed in semiconductor hosts having extended coherence times and optical accessibility are ideal candidates for quantum information and high-precision quantum sensing applications. For such platforms the quantum state can be compromised due to hyperfine-mediated couplings with the environmental nuclear spin bath (NSB) and the photon shot noise (PSN) entailed to the optical spin readout. The primary aim of this thesis is to employ well-established wavelet analysis techniques for exploring underlying quantum processes as well as suppressing classical and quantum noises. First, I investigate the NSB behavior with synchrosqueezed wavelet transform which reveals the time-frequency dynamics simultaneously, and hence locations and orientations of spinful nuclei relative to the central spin. Next, I tailor a wavelet-based approach, which I name as the template margin thresholding (TMT) method, to combat PSN for negatively-charged nitrogen-vacancy centers (NV^-) in diamond. Unlike the conventional frequency-based filters, TMT has an *unfair* advantage as it facilitates *on-resonant* frequency band denoising of the photoluminescence (PL) acquired. I show that the wavelet-based denoising can enhance the signal-to-noise ratio by an order of magnitude as I computationally demonstrate on NV-center magnetometry. However, the TMT-method starts to lose its advantage for high-time-budget applications due to inferior scaling with respect to the standard quantum limit, which is remedied by modifying TMT into a different framework.

Keywords: nitrogen-vacancy centers, photon shot noise, NV^- magnetometry, wavelet based photon shot noise suppression, Ramsey magnetometry, Hahn echo magnetometry.

ÖZET

DALGACIK TEMELLİ İŞLEM SONRASI TEKNİKLERİN KATI HAL KUANTUM ÖLÇÜMLEME UYGULAMALARI İÇİN GELİŞTİRİLMESİ

Ekrem Taha Güldeste
Fizik, Doktora
Tez Danışmanı: Ceyhun Bulutay
August 2024

Yarı iletken malzemelerde bulunan kusur merkezlerinin spin serbestliği, uzun eşevrelilik süreleri ve optik olarak ulaşılabilirliği sayesinde kuantum bilgi ve yüksek hassasiyetli kuantum öçümleme uygulamaları için ideal sistemlerden birisidir. Fakat bu tür platformlarda kuantum durumların nükleer spin hamamı ile girdiği en ince altyapı etkileşimleri ve optik okuma esnasında ortaya çıkan foton saçak gürültüsü nedeni ile barındırdığı zarar vermektedir. Bu tezin başat amacı, iyi bilinen dalgacık analizi tekniklerini kullanarak bazı kuantum süreçlerini keşfetmek ve bunun yanı sıra klasik ve kuantum gürültülerini baskılamaktır. İlk olarak, nükleer spin hamamı davranışları, zaman frekans dinamiklerini açığa çıkaran senkronsıkıştırmalı dalgacık dönüşümü ile irdelenmiştir. Ve bu şekilde nükleer spinlerin merkez spine bağıl olarak uzaklık ve yönelimleri saptanmıştır. Sonrasında, taslak sınır eşikleme (TSE) yöntemi olarak adlandırdığım, negatif yüklü nitrojen kusur merkezlerinde optik okuma sırasında açığa çıkan foton saçak gürültüsü ile mücadele etmek için dalgacık tabanlı bir yöntem tasarlanmıştır. Geleneksel frekans temelli filtrelerin aksine, TSE metodu toplanmış olan ışıma işaretini rezonans frekans bölgesinde de gürültüden arındırmaya imkan sağlaması bakımından bir hayli avantajlıdır. Dalgacık tabanlı gürültü giderme tekniğinin işaret-gürültü oranını on kata kadar nasıl geliştirilebilineceği manyetik alan öçümlemesi özelinde gösterilmektedir. Fakat, standard kuantum limitinden daha kötü ölçeklenmesinden ötürü, TSE metodu bu avantajını yüksek bütçeli işlerde kaybetmektedir. Bu kaybın TSE metodunun başka bir yaklaşımla ele alınması sayesinde nasıl telafi edildiği tezin son kısmında gösterilmektedir.

Anahtar sözcükler: nitrojen-deşik merkezleri, foton saçma gürültüsü, NV^- manyetometri, dalgacık tabanlı foton saçma gürültüsü baskılama, Ramsey manyetometrisi, Hahn yankı manyetometrisi.

Acknowledgement

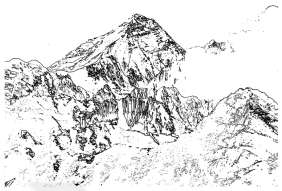

Good planning is important. I've also regarded a sense of humor as one of the most important things on a big expedition. When you're in a difficult or dangerous situation, or when you're depressed about the chances of success, someone who can make you laugh eases the tension.
— Sir Edmund Hillary

Foremost, I would like to express my deepest gratitude to my advisor, Prof. Dr. Ceyhun Bulutay for his guidance in the past years. So far, he has saved me from at least N avalanches, $N+1$ landslides, $N+2$ hurricanes, that occur ofttimes in a typical scientific expedition. Every bit of this journey has been a gift.

I would like to thank Prof. Dr. Mehmet Özgür Oktel and Prof. Dr. Ahmet Keleş for being in my TIK committee and for their insightful suggestions and comments during the last 4 years.

Next, I thank the rest of my Ph.D jury: Prof. Dr. Deniz Aybaş Tümtürk for sparing her valuable time, and Prof. Dr. Mehmet Emre Taşgın for his support from the day we met.

I also thank Prof. Dr. Oğuz Gülseren who always checks on me to see if I am okay whenever we meet in the corridor of the SA building.

I would like to express my sincere gratitude to Dr. Ali Sayir, the program manager of the Air Force Office of Scientific Research (AFOSR) project that has funded me for the past two years, for his confidence in me and our project, as well as for his patience and understanding during the lengthy article review process.

The original version of the image above taken from the source [1].

Chapter 3 of this thesis is partially supported by Türkiye Bilimsel ve Teknolojik Araştırma Kurumu (TUBİTAK) under Project No. 116F075.

Chapters 4, 5, and 6 of the thesis are an outgrowth of AFOSR funded project (FA9550-22-1-0444), entitled "Wavelet-Enhanced Quantum Sensing with Solid-State Nuclear Spins".

The numerical simulations reported in this thesis were partially performed at Türkiye Bilimsel ve Teknolojik Araştırma Kurumu (TUBİTAK) ULAKBİM, High Performance, and Grid Computing Center (TRUBA resources).

I acknowledge my old groupmate Mustafa Kahraman for his friendship and valuable discussions.

I would like to express my gratitude to my dear friends Fatih, Burak, Ömer Faruk, Selim Han, Hasan, and Mustafa for their enriching conversations over the years.

My heartfelt thanks go to our dear friends in Ankara, Taha and Şeyma, for always welcoming us with open arms and warm hospitality.

I am indebted to my parents, Hatice and Ayhan, my grandmother, Müşerref, my sister, İkbal Vildan, her husband Yasir Yılmaz, and youngest member of our beautiful family, Yusuf Kayra, my brother Mustafa Talha and his dearest child Zeynep Alya for their invaluable support. Without them it would be impossible to finish this thesis.

For Hilal . . .

Contents

List of Figures

List of Tables

Chapter 1

Introduction

There are three difficulties in authorship; to write anything worth publishing, to find honest men to publish it, and to find sensible men to read it.

— Charles Caleb Colton

The spin manifolds of semiconductor defects are multifaceted platforms for quantum metrology. However, their sensitivity is ultimately limited due to the coupling with a spin reservoir, which is formed by nuclear spins in the host lattice. Another fundamental limitation arises from the readout process of the physical quantity of interest, which is interrogated by defect spin. This thesis first aims to investigate the reservoir dynamics imprinted on the defect spin using a two-point correlation function, and extract spatial information about the positioning of the nuclear spins which can be silenced subsequently to improve the sensitivity. Following this, the bulk of the thesis suggests a wavelet based post-processing technique to suppress the shot noise entailed to the spin readout for negatively

The original version of the image above taken from the source [2].

charged nitrogen-vacancy (NV^-)

As for this introduction chapter, one of the main motives is to establish the *jargon* that I use throughout this dissertation such as *central spin, decoherence, photon shot noise, standard quantum limit, etc.,* that may pop up suddenly in the pages ahead. Additionally, with all due respect to those excluded, it serves to give some credit to a selective portion of the *quantum information* and *sensing* community whose works (among many others) helped me to understand *the sport* that I do so far. Therefore, in this chapter, I briefly mention the works that enlighten the spin dynamics of an electron confined in a semiconductor matrix and the developments in nitrogen-vacancy-based sensing techniques.

1.1 Electron and nuclear spin interface

A spin degree of freedom hosted by a semiconductor material is widely adopted across multiple fields from quantum computing [3, 4, 5], to quantum sensing applications [6, 7] among with many others such as quantum simulation, atomic clock transitions or time crystals [8, 9, 10]. These versatile areas of use originate from the compliance of a rule set known as the DiVicenzo criteria [11], as they possess well-isolated two-level systems with large coherence times [12, 13], and can be harnessed at high fidelity [14, 15, 16]. From a computational perspective, an electron spin confined in a semiconductor matrix that is coupled to a spin reservoir can be categorized under the so-called Central Spin (CS) model [17]. This coupling is essentially driven by the hyperfine mediated interactions between CS and the nuclear spin bath (NSB) [18, 19, 20, 21, 22]. Nuclear spin sites in the host lattice are also coupled to each other through dipole-dipole (d-d) interactions which overall form a bath for the CS [23], and, lead to a phase information loss which is embedded in the off-diagonal entries of CS density matrix. While the total effective magnetic field acting on the CS is known as the Overhauser field, the back-action of the CS on NSB is called the Knight field [24]. The d-d induced nuclear spin flips in NSB fluctuate the Overhauser field due to inhomogeneous hyperfine couplings and hence polarization of the CS state is prone to *leak out into*

the NSB [25, 26, 27, 28, 29]. The decoherence process is one of the main problems that limit the operation capacity of CS [30, 31, 32, 33, 7]. There are many approaches developed to combat the CS *dephasing* such as dynamical decoupling techniques [34, 35, 36, 37, 38, 39] or selective dipolar spin decoupling [40]. On the other hand, controlled polarization transfer from CS to a targeted proximal nuclear spin via hyperfine coupling is beneficial as a quantum memory [41, 42, 43, 44].

In contrast to forming a reservoir to the CS, the nuclear spins are a prominent choice for quantum registers in solid-state platforms due to their long-lasting coherence when compared to the electron spin degree of freedom [45, 46]. For *dense* spin environments as in quantum dots, information registration can be achieved through collective spin waves [47] and aggregated spin state transfer [48]. On the other hand for *sparse* spin textures such as defect centers, this is executed by embedding the CS information onto nearby nuclear spin [49, 50, 51, 52]. For NV^- centers, this is utilized for repetitive readout techniques for both proximate ^{13}C [53], and nitrogen atoms [54, 55]. It is also noteworthy that the large multiqubit spin register containing 10 spins is also realized [56].

The magnetic field imaging of nuclear spin environments or proximate structures is another field of research. In self-assembled InGaAs QD, the fingerprint inherited to the nuclear spins through strain and electric quadrupole moments is engineered to provide atomistic level structural information [57]. The defects are widely used in nanoscale NMR imaging as distinguished probes with numerous sensing and decoupling techniques [58, 59, 60, 61, 62]. From the very first quantum sensing applications [63], imaging with defect centers has been realized with approximately 10 nm resolution [64] and further improved with Fourier magnetic imaging [65]. The efforts regarding the 3D nuclear spin bath construction also need to be addressed [66, 67].

In all of these applications, a deeper understanding of the interplay between CS and NSB is compulsory in addition to the *intra* bath dynamics of the host material. Systems in which CS flips are suppressed due to large energy splitting

can be considered under the pure dephasing model [21, 68]. There are diversified options available to get a grasp of the CS dynamics which is connected to a spin reservoir such as pair correlation approximations [68, 69, 70], cluster expansion [71, 27], cluster correlation expansion (CCE) [72, 73] together with other similar methods [21, 74, 75, 76, 21]. Among these, CCE keeps its unique place thanks to its simplicity and versatility [77]. Notably, it is adapted to investigate entangled spin qubits [78] and generalized for gaining insight into the longitudinal relaxation of defects [79]. It is further employed in SiC divacancies [80, 81] and very recently integrated to simulate dissipative spin baths dynamics [82].

1.2 Nitrogen-vacancy centers in diamond for quantum sensing

NV^- centers [83] are common point defects in diamonds with C_{3V} point group symmetry which consist of two unpaired electrons possessing a total spin-1 quantum system [84] [1]. With features like optical preparation and readout [85], and long coherence times lasting up to a second [12] NV defects have garnered considerable attention. They are a prominent option for probing the physical quantities such as magnetic field textures [86], temperature [87, 88], strain [89], rotation [90], or field sensing [6, 91, 92]. The room temperature manipulation of NV-centers enable them to be used in various biomedical applications [93, 94].

The sensitivity of NV center is essentially bounded by two fundamental phenomena, the first one is the T_2 time which is characterized by the *decoherence* process described in Sec. 1.1, and the second one is the photon shot noise (PSN) associated with the optical spin readout. PSN diminishes with the square root of the number of repeated measurements, a natural consequence of the central limit theorem [95, 96]. This scaling ($M^{1/2}$, where M is the number of repeated measurements) is known as the standard quantum limit (SQL). Even though the

[1] There also exist a neutral NV center with single unpaired electron (NV^0), however as this thesis only focuses on NV^-, sometimes I omit the charge part $^-$ when I refer to the negatively charged NV's.

utilization of quantum mechanical sources such as *entanglement* of multiple spin sensors can allow one to surpass SQL, in general, such systems suffer from fast decoherence rates [33]. On the other hand, it has been claimed that SQL can be surpassed by the use of classical resources [95, 97].

To improve the sensitivity of NV based quantum sensors there has been a considerable amount of effort such as spin echo time enhancements [98], contrast improvement by excited-level anti-crossing [99], elevating spin collection efficiency [100], spin to charge conversion [101, 102], charge noise suppression [103], nuclear spin polarization [104], employment of double-quantum transitions [105, 106]. This list can be appended with, covariance magnetometry techniques [107], weak measurement protocols [108], and spin squeezing [109]. There are also Bayesian *post-processing* techniques available [110, 111, 112] along with the time-resolved spin readout [113]. Moreover, increasing the gate fidelity by noise filtering [16] or deep-learning boosted coherence protection [114] are also available approaches for improving the NV-center performance.

1.3 Wavelets, but why?

The complex interplay between CS and spin reservoir requires advanced techniques like wavelet analysis [115, 116] which is the preferred choice in this thesis. As it is a well-established theory, and widely used in image compression, edge detection, and signal denoising [117]. Additionally, it has played a significant role in the detection of gravitational waves [118] and used in the fast detection of temporal magnetic fields [119]. Recently, wavelet transform has been employed to extract correlated noise in a metal-oxide-semiconductor device [120]. Furthermore, the non-stationary characteristics of PSN [33, 7], limit the operation capacity of conventional frequency-based filters where wavelet-based approaches have an *unfair* advantage thanks to multi-axis resolution.

1.4 Rest of this thesis

In Chapter 2, I provide a quick tour of the wavelet theory. Chapter 3 discusses the NSB fluctuation analysis using synchrosqueezed wavelet transform, which provides insight into the relative spatial configuration of spinful nuclei. The NV-center-based DC and AC magnetic field sensing schemes are prescribed in Chapter 4. Chapter 5 explains a wavelet-based filter to combat the PSN associated with the optical spin readout of a single NV-center which I named as template margin thresholding (TMT) method. Apperantly the TMT method starts to lose its advantage in high-time budget applications. In Chapter 6, I address this issue and modify the *standard*-TMT with a *recursive*- approach and show its performance. Finally, in Chapter 7, I give some concluding remarks.

Chapter 2

Tour de wavelet: a prologue

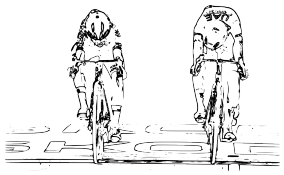

Science has never quite given man what he desired, not even in applied science. Man dreamt of wings; science gave him an easy chair which flies through the air.

— Denis Gabor

This chapter is intended to provide a rudimentary understanding of wavelets and not to drown the reader in the deep ocean of multi-resolution analysis. Therefore, it includes some basic intuition about why wavelets are important for a non-stationary signal analysis[1], as well as some variations of wavelet transforms and how to use them for signal enhancement. Even though the wavelet toolbox is well-established for signal processing, feature extraction, image compression, and many other branches of engineering, I believe this chapter might be a *sight for sore eyes* for a signal processing rookie (such as myself) who would like to take a

The original version of the image above taken from the source [121].

[1]Here, what is meant by the non-stationary signal is that the signal has varying mean and frequency features over time.

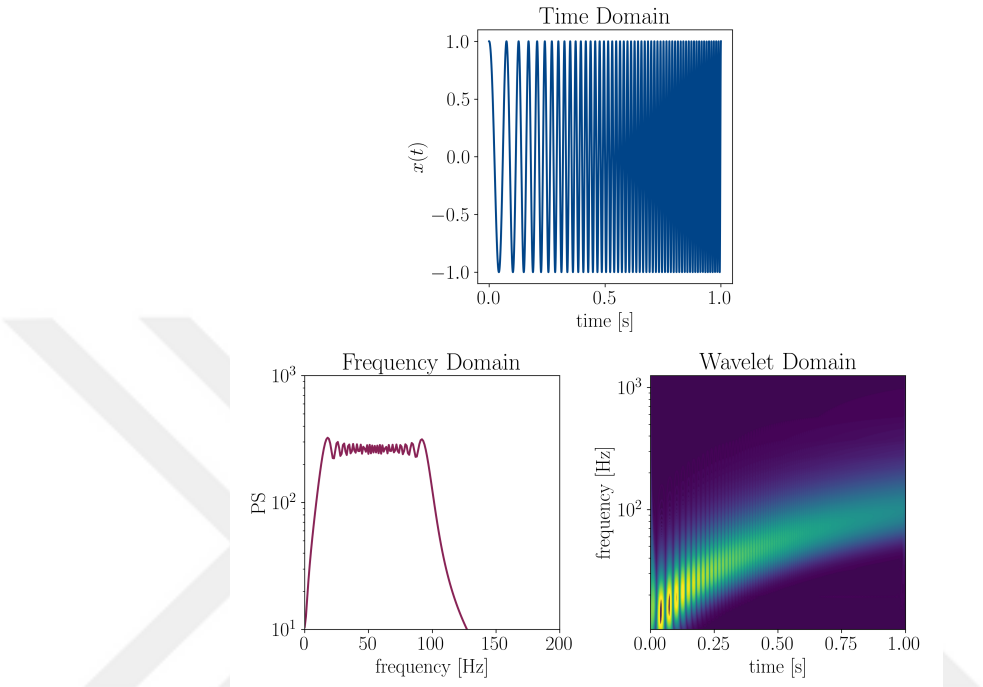

Figure 2.1: Frequency and wavelet representation of a chirped signal, $x(t)$.

glance at the wavelet theory. And of course, to make the following chapters more accessible.

2.1 Time-frequency analysis

2.1.1 Short time Fourier transform (STFT)

The Fourier transform of a signal, $x(t)$ can be expressed as,

$$X(f) = \int_{-\infty}^{+\infty} x(t) e^{-i2\pi ft} dt, \tag{2.1}$$

where $X(f)$ represents the signal in the frequency domain. As the standard Fourier transform utilizes the kernel $e^{-i2\pi ft}$ which extends to infinity in the time domain, the frequency representation, $X(f)$, does not carry any time information

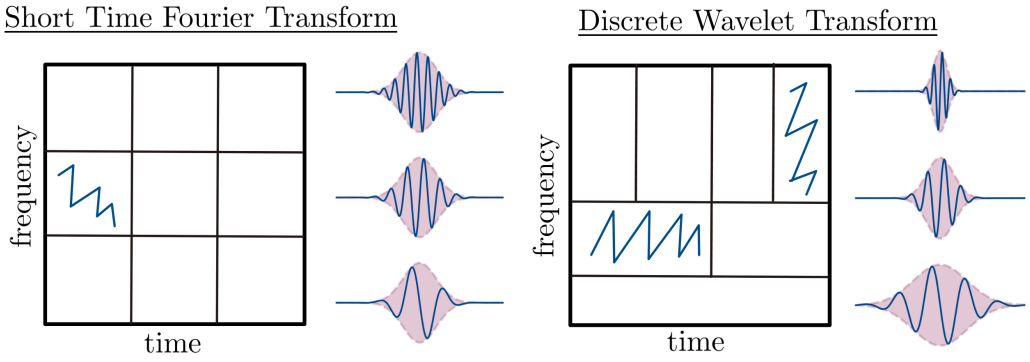

Figure 2.2: Time-frequency tiling of STFT (left) and DWT (right). STFT employs fixed windows, the DWT has varying window sizes that is, while for the high-frequency region, the size of the window is small, low-frequency region window size is large.

as it is integrated out. The use of time-frequency localized kernels to understand the behavior of non-stationary signals dates back to the 1940s. Instead of employing the standard Fourier transform, Denis Gabor multiplied the Fourier basis functions with Gaussian windows to extract the time features of non-stationary signals [117]. That is,

$$X(\tau, f) = \int_{-\infty}^{+\infty} x(t)u(t-\tau)e^{-i2\pi ft}dt, \tag{2.2}$$

where $u(\cdot)$ is the window function. The transformed function $X(\tau, f)$ now possesses also a time tag, τ. Eq. (2.2) forms a basis for the short-time Fourier transform (STFT) which is also known as the time-dependent Fourier transform.

2.1.2 Wavelet transforms

In the 1980s, the idea of STFT was extended with frequency-dependent windows to analyze seismic signals [122]. These frequency-*adapted* windows provide a superior multi-axis representation of the signals as they trade off finer time resolution with a coarser frequency resolution to capture highly oscillatory components of the signal and vice versa (see Fig. 2.1). It is possible to contrast the

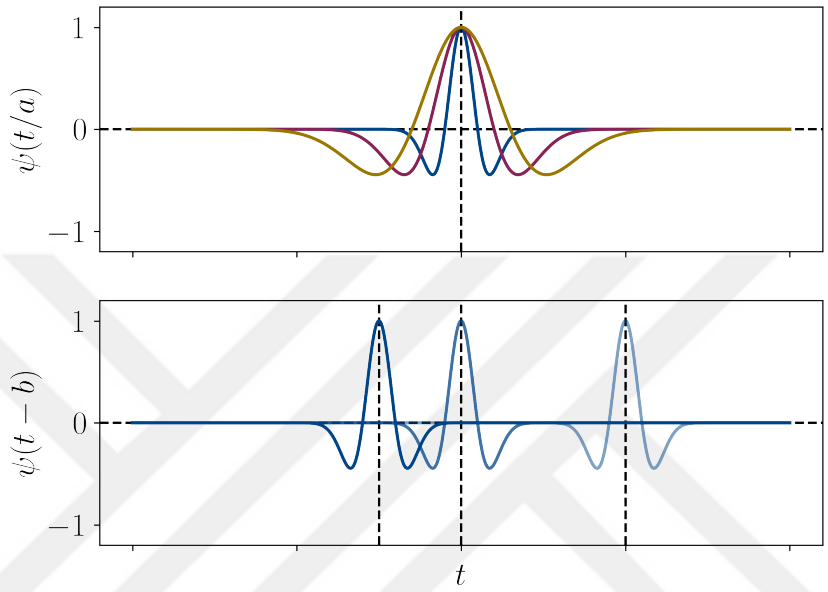

Figure 2.3: Mexican hat wavelet at different dilations a (upper panel) and translations (lower panel).

time-frequency tiles of constant and frequency-*adapted* windows in Fig. (2.2).

2.2 Continuous wavelet transform (CWT)

For a given signal, $x(t)$, which has finite energy $\left(\int_{-\infty}^{+\infty} |x(t)|^2 dt\right) < \infty$, can be mapped to the time-frequency domain as,

$$D(a,b) = \frac{1}{\sqrt{a}} \int_{-\infty}^{+\infty} x(t)\, \psi^* \left(\frac{t-b}{a}\right) dt, \tag{2.3}$$

where $\psi(\cdot)$ is the wavelet with scale parameter a and translation parameter b with a normalization factor $1/\sqrt{a}$. The wavelet function with scale a and translation k is written as,

$$\psi_{a,b}(t) = \frac{1}{\sqrt{a}} \psi \left(\frac{t-b}{a}\right) \tag{2.4}$$

in general, $\psi_{a,b}$ can have an imaginary part depending on the wavelet type, and the complex conjugate of $\psi_{a,b}$ is denoted by $\psi^*_{a,b}$. The scaling (dilation) parameter, a is a real number and is inversely proportional to the frequency which squeezes or stretches the wavelet. On the other hand, b translates the wavelet along the time axis (see Fig. 2.3). Since Eq. (2.3) is an inner product, it is also possible to express it by shorthand notation

$$D(a,b) = \langle x(t), \psi_{a,b}(t) \rangle \tag{2.5}$$

It should be noted that CWT is a highly redundant representation as a, b are continuous parameters and Eq. (2.3) should be calculated for every value of a given dilation and translation parameter. In general, representing a signal in wavelet the domain does not require this laborious work and can be accomplished utilizing Discrete Wavelet Transform (DWT) (see Sec. 2.3).

2.2.1 Synchrosqueezed wavelet transform (SWT)

The frequency axis resolution of the CWT can be improved by reassigning the instantaneous frequencies of the $D(a,b)$ through the synchrosqueezing wavelet transform (SWT) [115]. The instantaneous frequency can be calculated as,

$$d(a,b) = -i(D(a,b))^{-1} \frac{\partial}{\partial b} D(a,b), \tag{2.6}$$

with this instantaneous frequency, the SWT can be written as,

$$T(w,b) = \int_{A(b)} D(a,b) a^{-3/2} \delta\left(d(a,b) - w\right) da, \tag{2.7}$$

where $A(b)$ is the set of all possible scales a for which $D(a,b)$ is non-vanishing (i.e. $A(b) = \{a; D(a,b) \neq 0\}$). Eq. (2.7) reallocates the instantaneous frequencies by means of the Dirac delta function. As long as the frequency separation condition is satisfied, it is possible to increase frequency axis resolution while keeping time axis resolution intact as in Fig. 2.4. Even though the frequency resolution gets sharpened significantly it is possible to apply synchrosqueezing multiple times to increase frequency localization which is known as the multi-synchrosqueezing transform [123]. It should also be noted that the frequency

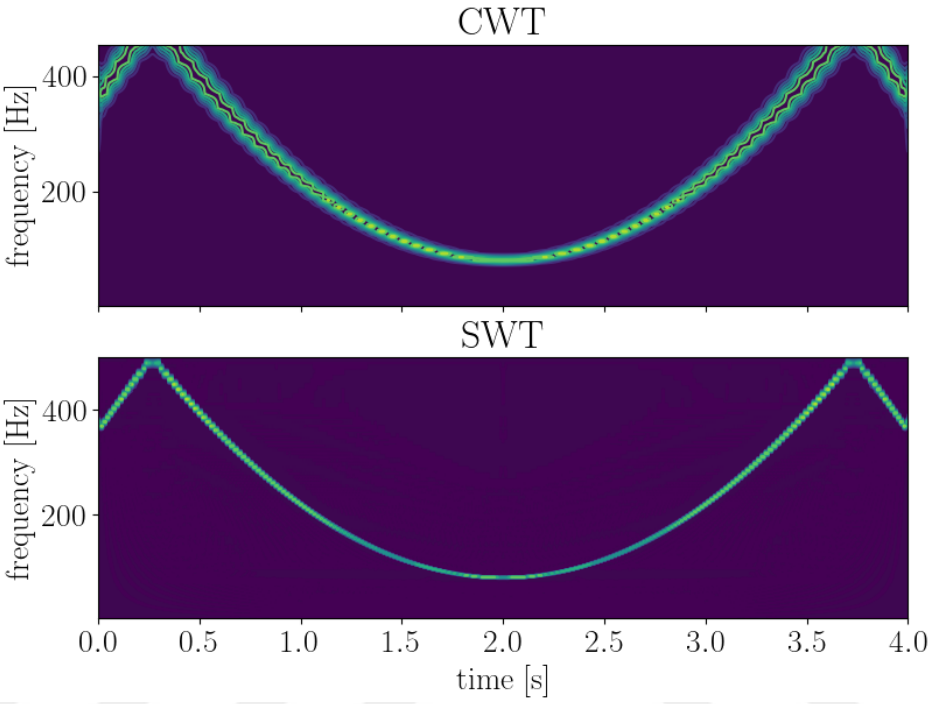

Figure 2.4: Continuous wavelet transform (upper panel) versus synchrosqueezed wavelet transform of a chirped signal (lower panel) with the so-called bump wavelet.

localization of both CWT and SST gets weaker in contrast to time localization for increasing frequencies. This is because of the multi-axis tiling scheme which is depicted as a cartoon in the right panel of Fig. 2.2.

2.3 Discrete wavelet transform (DWT)

In general, instead of utilizing the CWT, it is possible the represent a signal with less non-vanishing coefficients in the wavelet domain. If set of wavelets coefficients, constitute a *frame*, such that [124, 116],

$$AE \leq \sum_{n=-\infty}^{\infty} \sum_{n=-\infty}^{\infty} |d_{j,k}|^2 \leq BE, \tag{2.8}$$

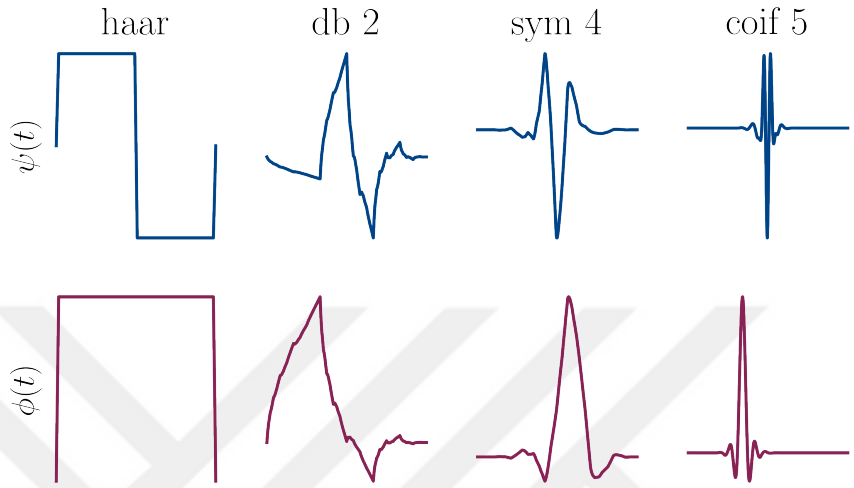

Figure 2.5: Various discrete wavelet types with corresponding scaling functions. From left to right, Haar, Daubechies-2, Symlet-4, Coiflet-5.

where, A and B are so-called frame bounds, and $E = \int_{-\infty}^{+\infty} |x(t)|^2$ is some finite signal energy, and $d_{j,k}$ is the discretized wavelet coefficients $d_{j,k} = \langle x(t), \psi_{j,k}(t) \rangle$ with[2],

$$\psi_{j,k}(t) = \psi\left(\frac{t - kb_0a_0^j}{a_0^j}\right) / \sqrt{a_0^j}, \tag{2.9}$$

so that the scale index j and the location index k are now integers instead of real numbers with scale and translation parameters, a_0 and b_0. If the *frame* is *tight* ($A = B$), then the signal, $x(t)$ can be reconstructed without loss of information,

$$x(t) = \frac{1}{A} \sum_{j=-\infty}^{\infty} \sum_{k=-\infty}^{\infty} d_{j,k}\, \psi_{j,k}(t). \tag{2.10}$$

However, if $A = B > 1$ the frame is considered to be a *redundant* one, and it is possible to find a frame in which $A = B = 1$ in which the family of wavelets $\psi_{j,k}$ form an orthonormal basis, and therefore can compactly represent the signal

[2]Wavelets represented by Greek letter ψ by convention. In the following Chapters, I also represent the state vector with $|\psi\rangle$. However, these two can be distinguished by notations "$\langle\cdot|\psi\rangle$" and "$\langle\cdot, \psi\rangle$" where the former represent a state vector, and the latter displays wavelet.

$x(t)$. So that,

$$\delta_{j,j'}\delta_{k,k'} = \int_{-\infty}^{\infty} \psi_{j,k}(t)\, \psi_{j',k'}(t)dt. \tag{2.11}$$

If we choose $a_0 = 2$ and $b = 1$ to dyadically grid the wavelet domain, it turns out that there exists a *fast* algorithm to calculate DWT (see Sec 2.3.1) with complexity of $\mathcal{O}(N)$ and it is cheaper than fast Fourier transform algorithm (FFT) with complexity of $\mathcal{O}(N \log N)$.

If the signal of interest, $x(t)$ has some non-vanishing DC value, the summation requires infinitely many wavelets which are of different scales, since $\int_{-\infty}^{+\infty} \psi_{j,k}(t)dt = 0$. To mitigate these infinite summations, another set of functions can be defined, $\phi_{j,k}$ with a non-vanishing mean. These functions are called the scaling functions which are orthogonal to wavelets functions at the same scale,

$$\langle \phi_{j,l}, \psi_{j,k} \rangle = \int_{-\infty}^{+\infty} \phi_{j,l}(t)\, \psi_{j,k}(t)dt = 0, \tag{2.12}$$

yet they form a basis for the wavelets in the coarser scale [117, 116],

$$\psi_{0,0} = \sum_k h_1(k)\sqrt{2}\phi_{0,0}(2t - k), \tag{2.13}$$

where $h_1(k)$ is the wavelet-dependent coefficient, and $\phi_{0,0}$ is the so-called, father wavelet. From this father wavelet, it is possible to generate coarser scaling functions as well,

$$\phi_{j,k} = 2^{-j/2}\phi(2^{-j}t - k), \tag{2.14}$$

so that a function of interest with $\overline{x(t)} \neq 0$ can be expressed without requiring an infinite sum of wavelets over different scales [3],

$$x(t) = \sum_{k=-\infty}^{\infty} c_{J,k}\phi_{J,k}(t) + \sum_{j=0}^{J}\sum_{k=-\infty}^{\infty} d_{j,k}\psi_{j,k}(t), \tag{2.15}$$

where, $c_{J,k} = \langle x(t), \phi_{J,k}(t) \rangle$, are called as *approximation* coefficients, and, $d_{j,k} = \langle x(t), \psi_{j,k}(t)$ are known as the *detail* (wavelet) coefficients. The decomposition in Eq. (2.15) is known as discrete wavelet transform or DWT.

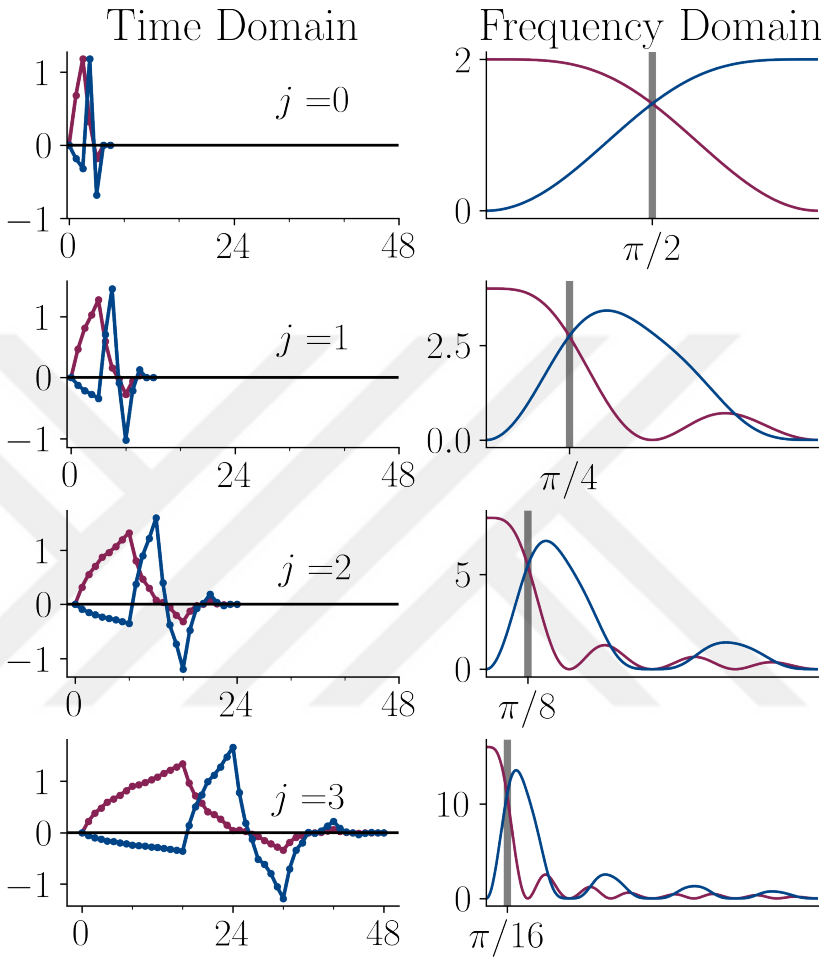

Figure 2.6: Time and frequency representation of db 2 wavelet at different scales. Red and blue lines represent the father and mother wavelets, respectively.

2.3.1 Fast wavelet transform (FWT)

For a discrete time series signal, S. Mallat has shown that DWT can be evaluated using half-band-lowpass and half-band-highpass filters [125, 126],

$$c_{j,k} = \sum_m h_0(m - 2k)\, c_{j-1,m}, \tag{2.16}$$

$$d_{j,k} = \sum_m h_1(m - 2k)\, c_{j-1,m}, \tag{2.17}$$

[3]The overbar represents the time average of signal x

where, $c_{j,k}$ ($d_{j,k}$) is the approximation (detail) coefficient at the detail level j and h_0 and h_1 are the lowpass and highpass filters respectively. It is important to note that the argument $2k$ in Eqs. (2.16) and (2.17) is to execute the decimation of the approximation and detail coefficients. The decimation throws away *redundant* coefficients since the higher half of the frequencies are already represented in the previous decomposition level and can be dropped without loss of information which is guaranteed by the Nyquist sampling theorem. This operation can be executed iteratively to reach a desired decomposition level and allows us to separate the signal into dyadically gridded frequency chunks as illustrated in Fig. 2.6.

2.3.2 Undecimated Wavelet Transform (UWT)

The decimation in Eqs. (2.16) and (2.17) disturbs the time invariance of the signal which is mapped into the wavelet domain. Fortunately, it is possible to recover time-invariance by moving to a *redundant* representation of the $x(t)$ at the expense of increasing computational complexity. This approach is widely employed for denoising purposes and is called undecimated wavelet transform (UWT)[4]. The UWT is a fast wavelet transform without the decimation.

2.4 Wavelet shrinkage

Wavelet shrinkage is a signal processing tool and a well-established method for compression of images (JPEG2000) or voice signals (MP3). The idea behind the wavelet *shrinkage* is to reassign values that are below a certain threshold value for each detail level to make data representation more *sparse* in the wavelet domain [127, 128, 129]. This approach is also used for the denoising of signals, if

[4]The undecimated wavelet transform is also called stationary wavelet transform or redundant wavelet transform by the wavelet community.

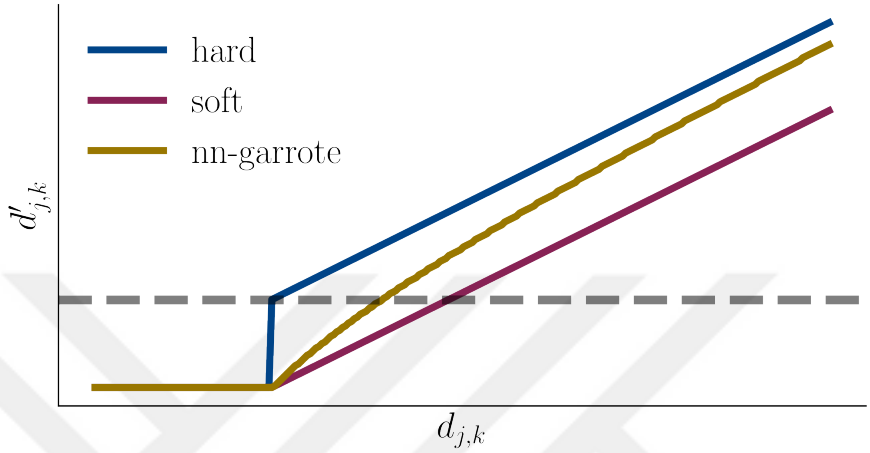

Figure 2.7: Common shrinkage methods: hard (blue), soft (red), and non-negative garrote (yellow). The dashed line represents the threshold value, horizontal and vertical axes are the detail coefficients before and after shrinkage, repectively.

it is disturbed by some noise source. For example,

$$d_{j,k}^{\text{hard}} = \begin{cases} |d_{j,k}|, & |d_{j,k}| > \lambda_j \\ 0, & |d_{j,k}| \leq \lambda_j \end{cases}, \tag{2.18}$$

is known as hard thresholding where λ_j is the threshold level for the jth detail level. There are other types of shrinkage methods as well,

$$d_{j,k}^{\text{soft}} = \begin{cases} \text{sgn}(d_{j,k})(|d_{j,k}| - \lambda), & |d_{j,k}| > \lambda_j \\ 0, & |d_{j,k}| \leq \lambda_j \end{cases}, \tag{2.19}$$

is called as soft thresholding, where $\text{sgn}(\cdot)$ is the signum function. Another popular choice is the shrinkage known as non-negative garrote [130],

$$d_{j,k}^{\text{garrote}} = \begin{cases} x - \dfrac{\lambda^2}{x} & |d_{j,k}| > \lambda_j \\ 0, & |d_{j,k}| \leq \lambda_j \end{cases}, \tag{2.20}$$

these are depicted in Fig. 2.7

Chapter 3

Nuclear spin fluctuations in spin defects

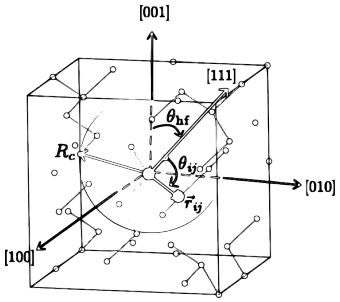

All models are wrong, but some are useful.
— George E. P. Box

This chapter is adapted from our publication [131].

As a first use case of wavelets, in this chapter, I have discussed the dipole-dipole (d-d) interactions of nuclear spin bath (NSB) which is imprinted on the central spin (CS) on the semiconductor solid-state matrix via a two-point correlation function. Each d-d induced contribution to the NSB dynamics is investigated with various computational-axes introduced by the external DC field alignment. The model is based on the Fermi-contact type hyperfine coupling between CS and background nuclear spins. By employing the SST of a given NSB fluctuation, it

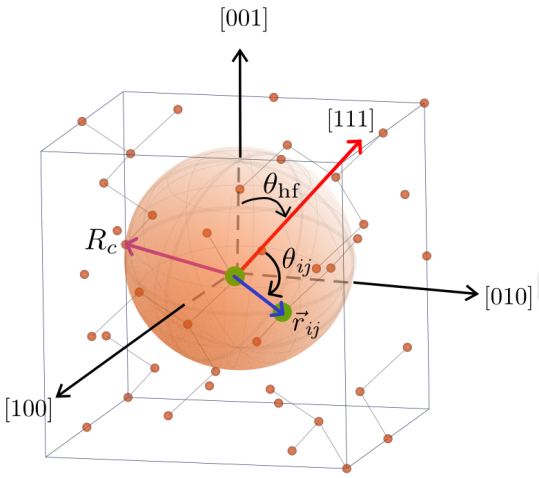

Figure 3.1: Typical solid-state spin environment. While the red arrow displays the quantization axis of the CS the blue arrow shows the displacement vector between two nuclear spins. $\theta_{\rm hf}$ is the angle between the [001] and quantization axis, and θ_{ij} is the angle between the quantization axis with displacement vector. R_c is the d-d interaction radius.

is possible to extract information regarding the neighboring cluster alignments and their relative positioning with respect to the CS.

3.1 Model Hamiltonian

The generic Hamiltonian for an electronic central spin (CS) that interacts with the nuclear bath spins in the solid-state matrix can be written as,

$$H/\hbar = -\gamma_e B_0 S_z + \vec{S} \cdot \sum A_j \vec{I}^j - \sum_j \gamma_j B_0 I_z^j + \sum_{i<j} \vec{I}^i \cdot \mathbb{D}_{ij} \cdot \vec{I}^j, \tag{3.1}$$

where γ_e (γ_j) is the gyromagnetic ratio of central (nuclear) spin, B_0 is the large bias field applied along the quantization axis of the central spin (CS), so that the effective Larmor frequency for central (nuclear) spin is $\omega_{\rm cs} = -\gamma_e B_0$ ($\omega_j =$

$-\gamma_j B_0$), the S and I^j are the spin operators for central and jth nuclear spin site in the nuclear spin background, respectively, and $\mathbb{D}_{ij}$ is the (d-d) coupling between the ith and jth nuclear spin site.

For typical III-V quantum dots or Si:P donors, if the bias magnetic field B_0 is large, the CS spin flip by hyperfine interaction is highly unlikely due to huge energy mismatch [69, 132]. Therefore, nonsecular hyperfine interactions can be safely dropped such that the hyperfine coupling becomes purely dephasing [133]. For a strong Zeeman interaction, adiabatic approximation allows us to drop the secular terms of d-d interaction [134, 135], but for bias field around 10 mT, I am going keep these terms in which the pure dephasing model for the CS is still valid [21, 136] and investigate the adiabatic approximation case separately.

As long as the CS flip is suppressed, the Hamiltonian in Eq. (3.1) can be conditioned on the CS states [137],

$$H^{\pm} = P_{\pm}\beta^z + \sum_{i<j} \vec{I^i} \cdot \mathbb{D}_{ij} \cdot \vec{I^j}, \tag{3.2}$$

here, $\beta^z = \sum_j \beta_j^z = \sum_j A_j I_z^j$ is the bath (Overhauser) operator, A_j and I_z^j are hyperfine coupling and the nuclear spin operator along the quantization axis (the hf-axis) for the jth nuclear spin site. Here, I drop the Zeeman couplings of the nuclear spins since they can be neglected for a relatively low bias field. The $P_{\pm} = \langle \pm | S_z | \pm \rangle$ with $|\pm\rangle$ is the CS state along the quantization axis. The d-d interaction can be expanded through the so-called dipolar alphabet [134, 135],

$$\sum_{i<j} \vec{I^i} \cdot \mathbb{D}_{i,j} \vec{I^j} = \sum_{i<j} \frac{\mu_0}{4\pi} \frac{\hbar^2 \gamma_i \gamma_j}{|\vec{r}_{ij}|^3} \left(\mathcal{A} + \mathcal{B} + \mathcal{C} + \mathcal{D} + \mathcal{E} + \mathcal{F}\right), \tag{3.3}$$

here, μ_0 is the permeability of vacuum, and $\vec{r}_{ij}$ is the displacement vector that connects nuclear spin sites i and j. These dipolar alphabet terms $(\mathcal{A}, \mathcal{B}, \mathcal{C}, \mathcal{D}, \mathcal{E}, \mathcal{F})$ can be written explicitly as,

$$\mathcal{A} = I_z^i I_z^j (3\cos^2\theta_{ij} - 1), \tag{3.4a}$$

$$\mathcal{B} = (I_+^i I_-^j + I_-^i I_+^j)\frac{1 - 3\cos^2\theta_{ij}}{4}, \tag{3.4b}$$

$$\mathcal{C} = (I_+^i I_z^j + I_z^i I_+^j)\Big(\frac{3}{4}\sin 2\theta_{ij}\Big)e^{-i\phi_{ij}}, \tag{3.4c}$$

$$\mathcal{D} = (I_-^i I_z^j + I_z^i I_-^j)\Big(\frac{3}{4}\sin 2\theta_{ij}\Big)e^{+i\phi_{ij}}, \tag{3.4d}$$

$$\mathcal{E} = I_+^i I_+^j \Big(\frac{3}{4}\sin^2\theta_{ij}\Big)e^{-2i\phi_{ij}}, \tag{3.4e}$$

$$\mathcal{F} = I_-^i I_-^j \Big(\frac{3}{4}\sin^2\theta_{ij}\Big)e^{+2i\phi_{ij}}. \tag{3.4f}$$

here, I_+ and I_- are spin creation and annihilation operators, θ_{ij} and ϕ_{ij} are polar and azimuthal angles characterized by the quantization axis and $\vec{r}_{ij}$; see Fig. 3.1.

The nuclear spin fluctuations interacting with a spin qubit can written as a two-point correlation function,

$$C(t) = \langle \beta^z(t)\beta^z(0)\rangle = \langle e^{iH_e t}\beta^z e^{-iH_e t}\beta^z(0)\rangle \tag{3.5}$$

where H_e is the effective Hamiltonian which can be written by averaging Overhauser fields [137],

$$H_e = \frac{|P_+| + |P_-|}{2}\beta^z + \sum_{i<j}\vec{I}^i \cdot \mathbb{D}_{ij} \cdot \vec{I}^j \tag{3.6}$$

3.2 Further model details

Hyperfine coupling of the spinfull nuclear site in the lattice is determined by the proximity of nuclear spin to the CS. This Fermi-contact type coupling shows dramatic variations depending on the wavefunction envelope of the electronic spin degree of freedom and affects the decoherence process [20, 138, 139]. Throughout this chapter, I consider that the hyperfine couplings distributed according to,

$$A_i = A_0 e^{-r_i^2/L_0^2}, \tag{3.7}$$

here, A_0 is the maximum hf-coupling amplitude, r_i is the distance between CS and ith nuclear spin site, L_0 is the electron confinement radius which is set to be

3.4 nm. I choose, A_0, 10^4 times larger than the d-d coupling of nearest neighboring nuclear spins sites which can be written as,

$$E_{\text{d-d}} = \frac{\mu_0}{4\pi} \frac{\hbar^2 \gamma_i \gamma_j}{(a_0\sqrt{3}/4)^3}, \tag{3.8}$$

where a_0 is the lattice constant in the diamond crystal. As a nuclear spin environment, it is possible to consider a lattice box of dimensions $10\ a_0 \times 10\ a_0 \times 7\ a_0$ so that there are 5600 nuclear lattice sites available. Since typical defect concentrations are low (just a few ppm levels) [140], a CS that is positioned at the origin of such a box can safely mimic a realistic NSB. For group-IV semiconductors the typical natural abundance of spinfull nuclear spin sites are $\rho \approx 0.05$ for ^{29}Si with spin-1/2 [20], and $\rho \approx 0.01$ for ^{13}C which also has spin-1/2 [52]. Depending on the host matrix considered the lattice constant, a_0 is adjusted accordingly. To simulate this type of NSB fluctuations the cluster correlation expansion (CCE) is a suitable approach [137, 72, 73, 77]. I assume that the NSB is a thermal ensemble with infinite temperature so that $\rho = \otimes_i^N \mathbb{I}_i/2^N$ where, $\mathbb{I}_i$ is the identity matrix of ith nuclear spin.

3.3 Dipole-dipole transitions of a two spins cluster

In Fig. 3.2, the energy level diagram for the two nearest nuclear spin sites is shown when they have exactly the same hyperfine couplings $\Delta_{hf} = 0$, and when the displacement vector r_{ij} is along [111] direction so that the polar angle between the quantization axis and the displacement vector is $\theta_{ij} = 54.7$, the energy level $|m_F = 0\rangle$ becomes 2-fold degenerate. This degeneracy is lifted when there is a detuning between the neighboring hf-coupling constants and when the $\mathcal{A}$ in Eq. 3.4 becomes non-vanishing, as these are the diagonal entries of the environmental Hamiltonian. If these states are non-degenerate, then the zero-quantum (0Q, $\Delta m_F = 0$) transitions become available through the $\mathcal{B}$ term which induces total spin conserving transitions. As indicated by Fig. 3.2 there are also single-quantum (1Q, $\Delta m_F = 1$) and double-quantum (2Q, $\Delta m_F = 2$) transitions that are triggered by the dd-alphabet terms, $\mathcal{C}, \mathcal{D}$ and $\mathcal{E}, \mathcal{F}$ terms, respectively.

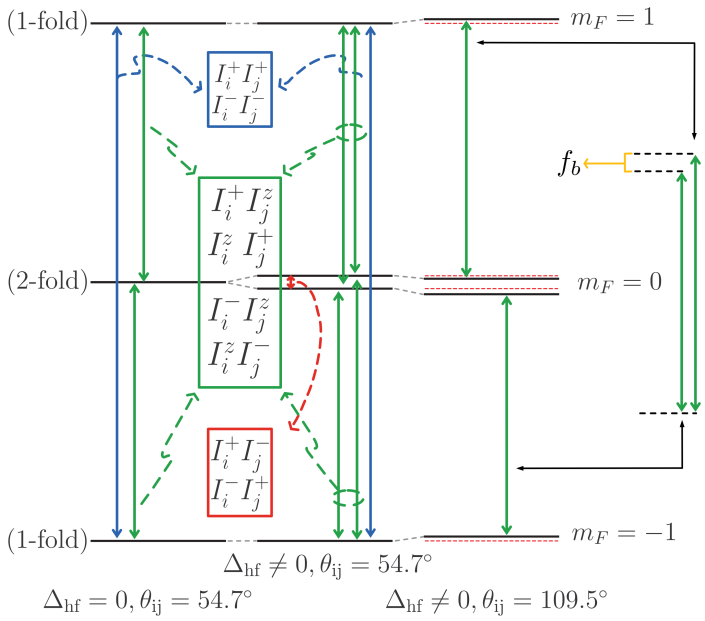

Figure 3.2: Energy level diagram for two nearest neighboring nuclear spin sites under different $\Delta_{\rm hf}$, θ_{ij} values.

3.4 Time-frequency behavior

The two-point correlator, $C(t)$ practically imprints the transitions with various Δm_F values, induced by the dd alphabet if not masked by the angle, θ_{ij}. My rationale was that the spectro-temporal behavior of the correlator can be uncovered in the wavelet domain, through CWT-based techniques (see Sec. 2.2). For this purpose, I have picked the bump mother wavelet as it has a better frequency resolution [141]. However, before the wavelet transform analysis, I normalize the correlator as,

$$\bar{C}(t) = \frac{C(t) - \langle C(t) \rangle_t}{C(0) - \langle C(t) \rangle_t}, \tag{3.9}$$

where, $\langle \cdot \rangle_t$ denotes the time average. For the sake of simplicity it is convenient to work with normalized time and angular frequency so that $\bar{t} = t\bar{A}$ and $\bar{\omega} = \omega/\bar{A}$, in which the mean value of hyperfine couplings sets the normalization parameter, $\bar{A} = \frac{1}{N}\sum_i A_i$.

In Fig. 3.3, two-point correlator of spin-1/2 nuclear spin sites are displayed

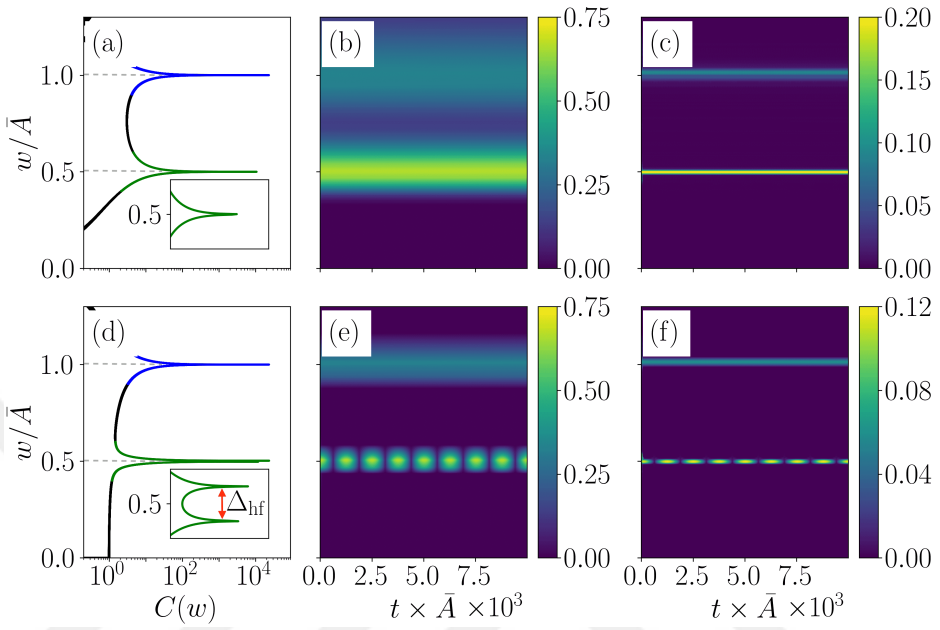

Figure 3.3: Fourier transform (first column), continuous wavelet transform (CWT) (second column) and synchrosqueezed wavelet transform (SST) (third column) of two nuclear spin-1/2 correlator $C(t)$ for θ_{hf}. The upper panel displays $\Delta_{\mathrm{hf}} = 0$, whereas lower panel shows $\Delta_{\mathrm{hf}} = 0.01\bar{A}$.

in Fourier and wavelet domain. Thanks to the normalization, $\bar{A}$ the 1Q and 2Q transitions can be identified at $\bar{\omega} = 0.5$ and $\bar{\omega} = 1$ respectively. The so-called flip-flop terms due to the dipolar alphabet term, $\mathcal{B}$, which typically occur near $\bar{\omega} = 0$ are not operative due to the alignment of the displacement vector with respect to the hyperfine axis, $\theta_{ij} = 54.7°$. It should be noted that when there is a hf-coupling detuning ($\Delta_{\mathrm{hf}} \neq 0$) the beating pattern appears due to the probability amplitude interference (see Fig. 3.3 (e)). Furthermore, as discussed in Chapter 2, the frequency localization gets weaker for high-frequency regions. However, for the remainder of this chapter, I will employ SST as in Fig. 3.3 (c) and (f) to have improved frequency resolution.

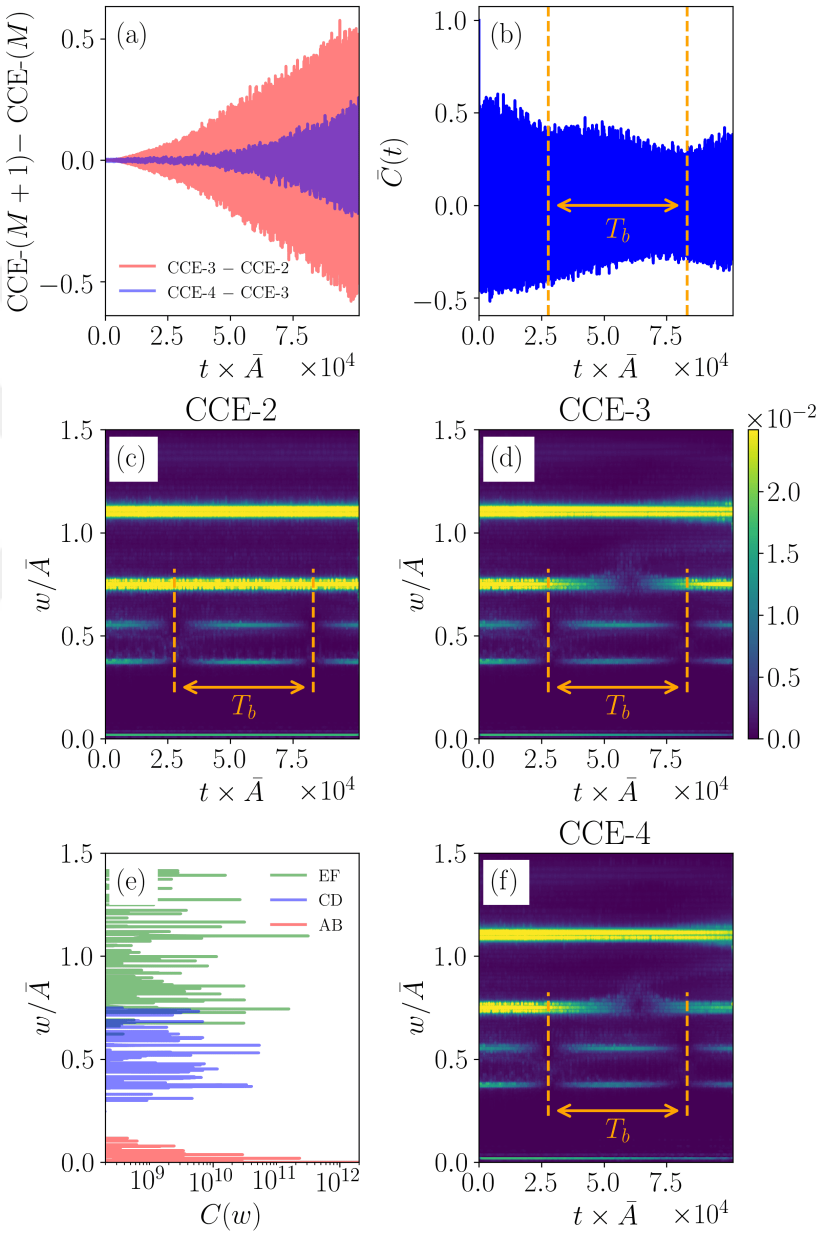

Figure 3.4: The NSB fluctuations with $\bar{A} \approx 13.5$ MHz(a), $\sigma_{\text{hf}} \approx 0.25\bar{A}$, $\theta_{\text{hf}} = 54.7°$, $\rho = 0.02$, $a_0 = 0.54$ nm and $R_c = 2.7a_0$. Convergence of $\bar{C}(t)$ at different CCE truncations. (b) time series representation of $\bar{C}(t)$ with CCE-4. (c), (d) and (f) are the wavelet representation of the time series $\bar{C}(t)$ for CCE-2, CCE-3, and CCE-4 respectively. Lastly (e) displays the power spectrum.

3.5 Convergence of cluster correlation expansion

Since CCE truncates the d-d coupled nuclear spin bath with maximum cluster size, the order of CCE should be decided according to the time scale of interest, along with the cutoff radius R_c. To be able to parse long-time dynamics effectively, one needs to increase CCE order as many body couplings start to dominate the spin fluctuation dynamics. This is actually illustrated in Fig. 3.4 (a), while the short-time dynamics well are described by CCE-2 (pair-correlations), They start to deviate from high-order CCE calculations for the late-time spin fluctuations. The other parameter that needs to be taken into account in determining the maximum cluster size is ρ. The NSBs considered in this chapter are relatively *sparse* in terms of spinfull nuclei [142], they are spatially isolated and CCE calculation with relatively small (3-4) cluster size essentially suffice to get convergent results. This can also be observed from comparing Fig. 3.4 (c), (d) and (f), while two 1Q beatings which have the period $T_b = 1/f_b$, due to small hf detuning of proximite spin sites (see Fig. 3.2) visible in the wavelet domain for all CCE orders, the beat around $\bar{w} = 0.75$ is captured by CCE-3 and CCE-4 simulations.

Apart from CCE cluster size, the other truncation that I briefly discussed in Sec. 3.2 is the computational box size considered during the simulations. The hf coupling rapidly drops after a few electron confinement radii, therefore, increasing the computational box size does not change the patterns appearing in the wavelet representation for the time scale of interest. Therefore, I confine the calculations in this chapter to the NSB described in Sec. 3.2.

3.6 Hyperine axis dependence

The quantization axis introduced by bias field direction, determines the nuclear spin noise accumulated in the CS state. To make quantum channels identifiable, I turned on and off the transition inducing dd-alphabet terms $\mathcal{B}, \mathcal{C}, \mathcal{D}, \mathcal{E}, \mathcal{F}$ and distinguished them by colors in the left column of Fig. 3.5. The power spectrum

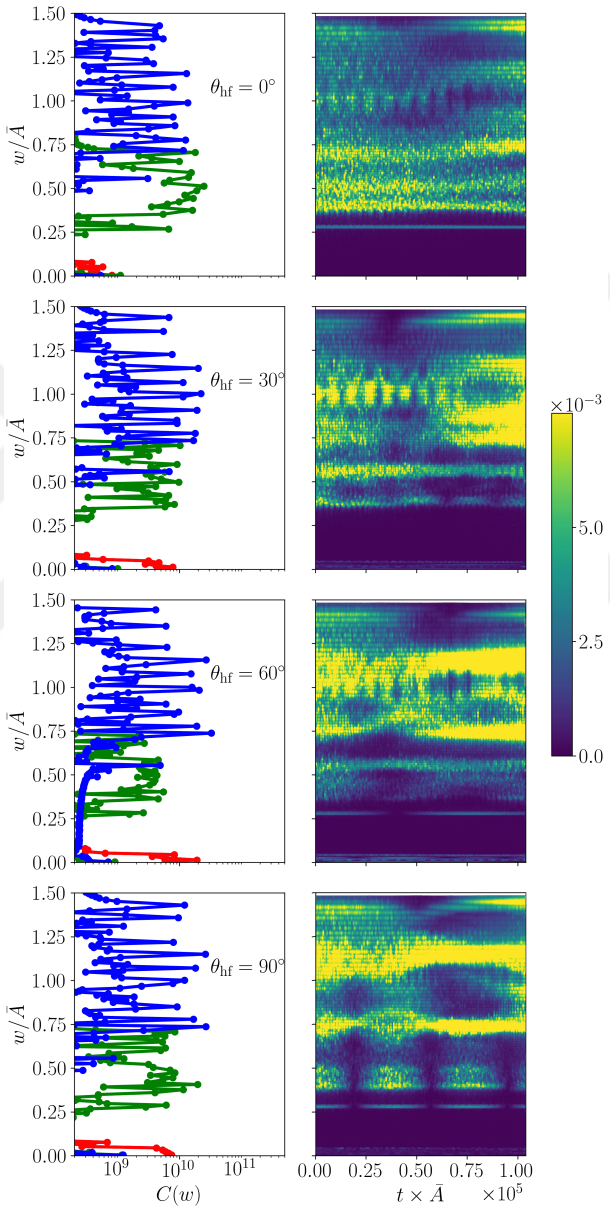

Figure 3.5: Power spectrum and corresponding SSTs of NSB fluctuations under different hf-axes for $\bar{A} \sim 13.9$ MHz, $\sigma_{\rm hf} \sim 0.25\bar{A}$, $N = 280$, $\rho \sim 0.05$, $a_0 = 0.54$ nm, $R_c = 2.0a_0$ with CCE order 3. While the left column displays the power spectra, the right column displays the SSTs. The coarse-grained contributions from dd-alphabet terms are shown with distinguished colors ($\mathcal{B}$ red line, $\mathcal{C}, \mathcal{D}$ green line, $\mathcal{E}, \mathcal{F}$ is the blue line.)

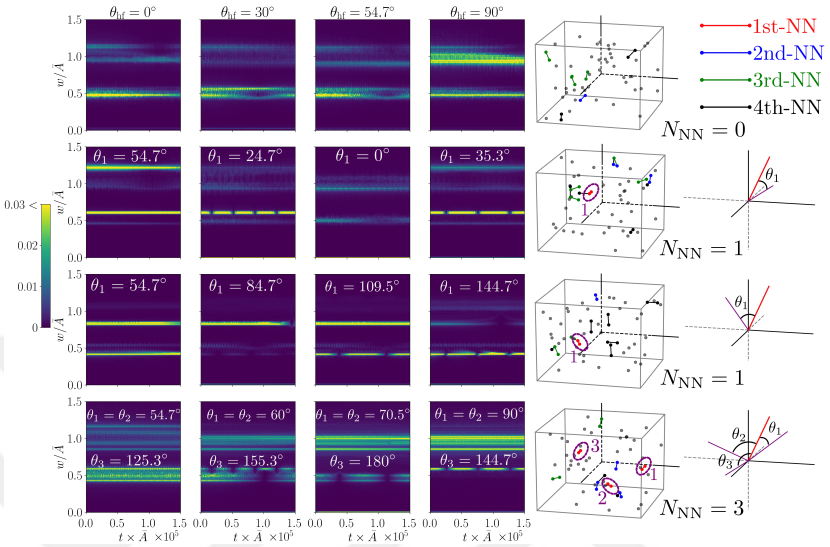

Figure 3.6: SST scalogram of the two-point correlator of various NSB realizations for various θ_{hf}. Here distinct bath realizations are shown for each row with, $N = 56$, $\rho = 0.01$, $a_0 = 0.35$ nm, $R_c = 2.5a_0$, $\bar{A} = 104$ MHz, $\sigma_{\text{hf}} = 0.12\bar{A}$. The fifth column shows the spatial distributions of different realizations in which the neighboring spin sites are encircled. The sixth column illustrates displacement vectors of the nearest-neighbouring spin sites.

for 0Q, 1Q, and 2Q channels drastically changes according to the quantization axis alignment. The behavior of this type is also illustrated in Ref. [27] for Hahn echo magnetometry decay under the secular approximation.

For $\theta_{\text{hf}} = 0°$, the 0Q dephasing channel is highly suppressed as the term $\mathcal{B}$ is significantly turned off which induces flip-flop transitions for nearest neighboring spin clusters. As illustrated in SST scalograms, while some of the 0Q and 1Q beatings become distinguishable as θ_{hf} deviates from 0°, the 2Q channel shows complex behavior for relatively high nuclear spin abundance ratio.

3.7 Different nuclear spin bath realizations

Next, I would like to draw attention to different NSB spatial distributions with relatively low spinfull nuclear abundance as in ^{13}C isotope in diamond. The features of the displacement vector that connects the nuclear spins within the proximity are imprinted in SST scalograms depending on the hf-axis. To show these features, I demonstrate different NSB realizations at each row in Fig. 3.6. The spinfull nuclear spin sites are marked with dots, and neighboring spins up to the fourth nearest neighboring spins are connected with distinct colors.

In the top row, there are no nearest neighboring nuclear site occurrences, and all features imprinted are essentially due to the second and third nearest neighboring spins. For the second row, there is only 1 nearest-neighbouring spin cluster which is imprinted by $\theta_{\mathrm{hf}} = 30^{\circ}$ and $\theta_{\mathrm{hf}} = 90^{\circ}$. This beating pattern disappears in the third column of Fig. 3.6, as the $\mathcal{C}$ and $\mathcal{D}$ vanishes in the dd-alphabet alphabet. It should be noted that the cluster in the first realization has an identical alignment to the 3rd cluster in the fourth realization and therefore has identical beating patterns. The cluster in the third realization can be distinguished for example, $\theta_{\mathrm{hf}} = 30^{\circ}$.

Overall, it is possible to distinguish the spatial positioning and orientation of the spin clusters thanks to the *good* frequency resolution with SST. Since, the Fermi-contact type of hf coupling depends on the spatial distance to the CS, the beat or stripe pattern appearing in the scalogram yields the information regarding the position and alignment.

3.8 High magnetic field regime

Now, I would like to focus on the 0Q transitions, of the last realization of Fig. 3.6 under the large magnetic filed regime with three nearest-neighbouring clusters. In the left column, I have plotted spin-1/2 NSB, since there is a single transition available for each spin cluster horizontal stripes appear in the scalogram. In the

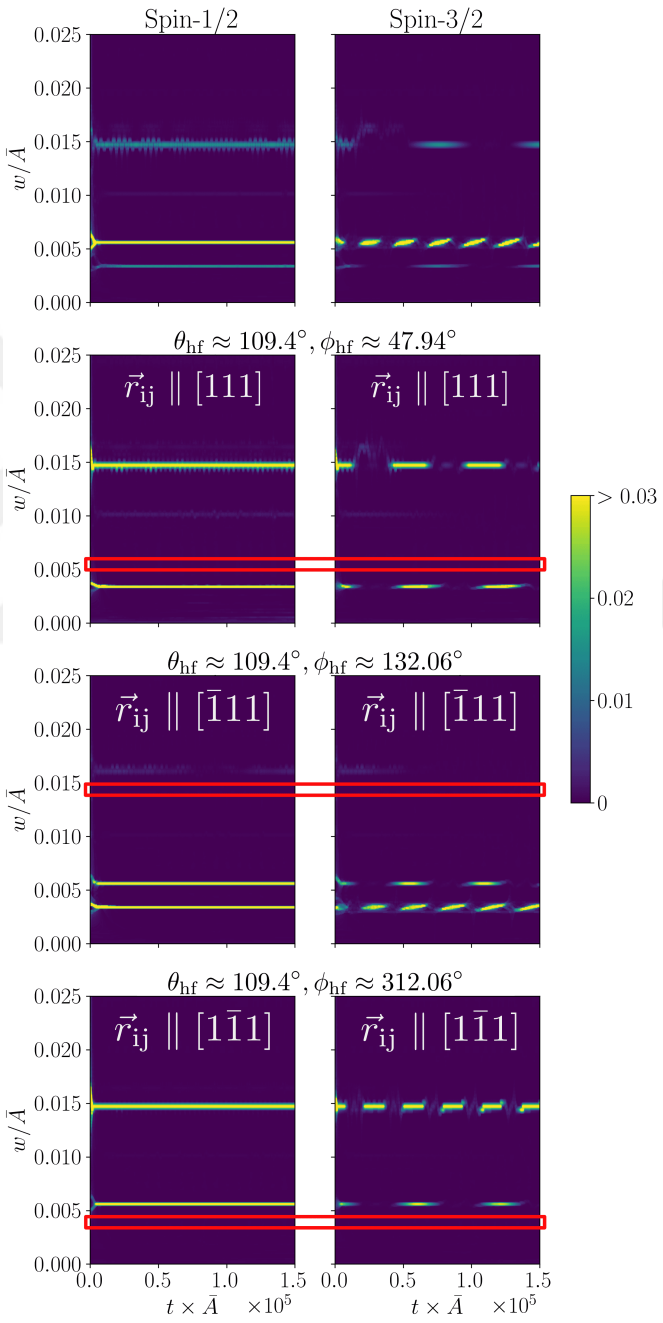

Figure 3.7: 0Q transitions of the fourth realization shown in Fig. 3.6 in large magnetic field regime. While the left and right columns show spin-1/2 and spin-3/2 realizations respectively. Each row displays specific $\theta_{\rm hf}$ alignment.

right panel, on the other hand, the beating patterns are visible for spin-3/2.

It is possible to extract information regarding the displacement vector alignment of the clusters. This can be achieved by first, calculating the SST of [001] and [111] hf-axis directions, as the hf-axis aligned with the [001] direction the first nearest-neighboring spin clusters has no contribution to the SST scalogram. When the hf-axis aligned in [111] directions all of the first nearest neighboring clusters contribute to the scalogram as indicated in the first row of Fig. 3.7 (see the stripes/beatings around $\bar{w} = 0.004$, $\bar{w} = 0.006$ and $\bar{w} = 0.015$). Second, arrange the hf-axis so that the angle between the displacement vector and hf-axis is 54.7°, and third repeat this process for each bond axis possible as indicated in Fig. 3.7.

3.9 Noise resilience of coherence beating in the wavelet scalograms

The model in Eq. 3.1 can be extended to cases for which quadrupolar interactions are involved for $I \geq 1$ [143], electron co-flip involved dynamic nuclear polarization models [43] or long-range hyperfine interactions [136]. To show the noise resilience of SST scalograms, I have disturbed the model Hamiltonian with random telegraph noise (RTN) to account for the charge noise [144]. I have introduced the stochastic Hamiltonian term,

$$\Xi(t) = \sum_{i=1}^{N} \nu_i \xi_i(t) I_z^i, \tag{3.10}$$

to the eq. (3.6), here ν_i is the amplitude of noise with Gaussian random variable, ξ_i is the binary switching function with rate Γ. It is possible to introduce the parameter $\eta = \bar{\nu}/\Gamma$ to characterize strong ($\eta \gg 1$) and weak ($\eta \ll 1$) coupling regimes of RTN [145]. Again, the fourth realization of Fig. 3.6 is employed in the 3.8, in (b) and (d) we the weak coupling ($\eta \approx 0.01$) which satisfies the Gaussian limit [37, 144, 145] and strong coupling ($\eta \approx 100$) regimes are used. The noisy SSTs are denoised to a huge extent thanks to undecimated wavelet transform

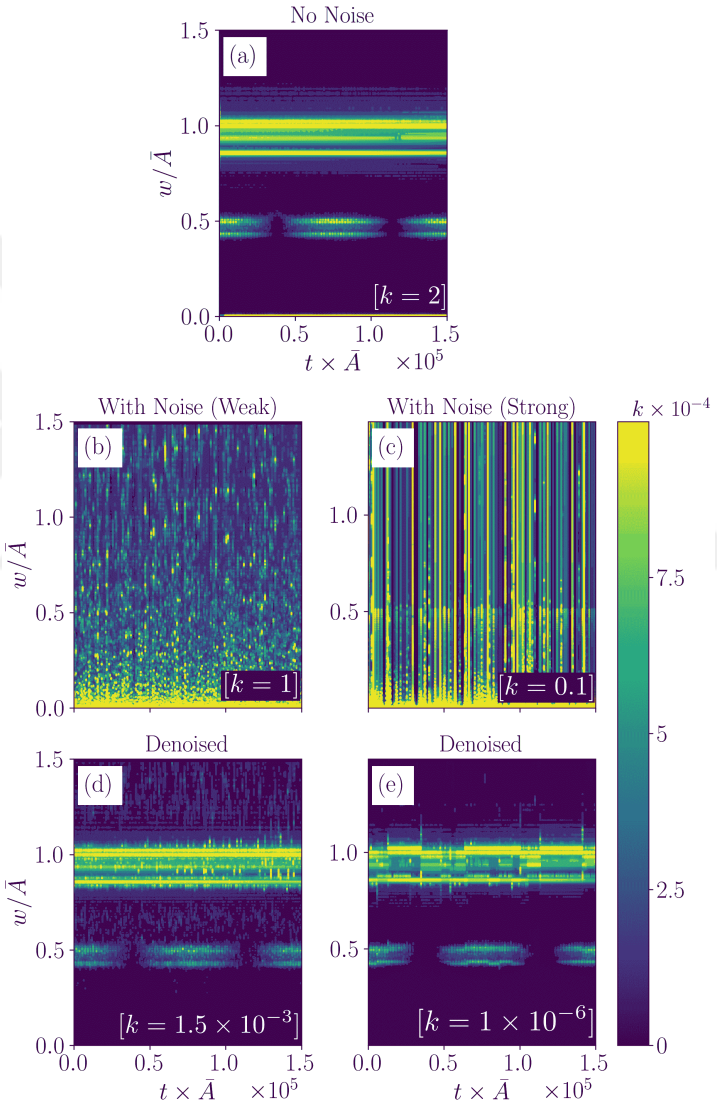

Figure 3.8: Fourth realization of Fig. 3.6 for $\theta_{\text{hf}} = 54.7°$. While (a) shows noiseless SST, the weakly $\eta \approx 0.01$ and strongly $\eta \approx 100$ coupled RTN are displayed in (b) and (c) respectively. The mean value for fluctuation coupled strength $\bar{\nu}$ and Γ are chosen to be $1 \times 10^{-2}\bar{A}$ and 10 kHz for strong coupling regime whereas $10^{-5}\bar{A}$ and 100 kHz for weak coupling regime. The subplots (d) and (e) are associated UWT filtered SSTs.

(UWT) by Haar wavelet decomposition as can be observed from (d) and (e).

Chapter 4

Magnetometry with a single nitrogen-vacancy (NV) centers

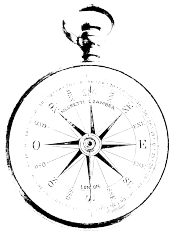

Statistics is the grammar of science. A scientific investigation should involve the recognition and formulation of a problem, the collection of data through observation and experiment, and the creation and evaluation of an explanatory model. Without data, you are just another person with an opinion, but the application of sound statistical principles can turn data into useful information and thereby into knowledge.

— Karl Pearson

The original version of the image above taken from the source [146].

The two fundamental phenomena that limit the sensitivity of NV-based quantum magnetometer are *sensor decoherence* and *shot noise* [33, 7]. While the former is due to the environmental coupling of the spin sensor, the latter originates from the projective optical spin readout of the NV-center. This chapter, first briefly discusses the dephasing mechanism due to nuclear ^{13}C spins in the diamond matrix with a single NV-defect. Then, describes the Ramsey and Hahn echo magnetometry schemes for sensing of DC- and AC- fields, respectively. Moreover, the framework to calculate the shot noise associated with the optical readout and magnetic field estimators is also provided.

4.1 Decoherence mechanism of single NV centers

The NV-center spin Hamiltonian can be split into three parts,

$$H = H_{\mathrm{NV}} + H_{\mathrm{int}} + H_{\mathrm{env}}, \tag{4.1}$$

here, H_{NV}, is NV-center Hamiltonian which contains the electron and nitrogen spin interactions, H_{int}, describes the coupling between the sensor spin with the spinful nuclei in the semiconductor matrix, and H_{env} is the term which characterizes the bath dynamics. Under bias magnetic field $\vec{B}_0$, the Hamiltonian terms can be written as [147],

$$\begin{aligned} H_{\mathrm{NV}}/\hbar = {} & DS_z^2 - \gamma_e \vec{B}_0 \cdot \vec{S} + \epsilon(S_x^2 - S_y^2) \\ & - \gamma_N \vec{B}_0 \cdot \vec{I} + \vec{I} \cdot \mathbb{P} \cdot \vec{I} + \vec{S} \cdot \mathbb{A} \cdot \vec{I}, \end{aligned} \tag{4.2}$$

$$H_{\mathrm{int}}/\hbar = \sum_{i=1}^{N} \vec{S} \cdot \mathbb{A}_i \cdot \vec{I}_i, \tag{4.3}$$

$$H_{\mathrm{env}}/\hbar = -\gamma_c \vec{B}_0 \cdot \sum_{j=1}^{N} \vec{I}_j + \sum_{i<j} \vec{I}_i \cdot \mathbb{D}_{ij} \cdot \vec{I}_j, \tag{4.4}$$

here, D is the zero field splitting, γ_e (γ_N) is the electron (nitrogen) gyromagnetic ratio, ϵ is the strain induced anisotropy, $\mathbb{P}$ and $\mathbb{A}$ are the quadrupolar[1] and hyperfine interaction tensors. The γ_c is the gyromagnetic ratio of the ^{13}C isotope

[1]This term is available for ^{14}N as it posses spin-1 system, whereas ^{15}N izotope has spin-1/2.

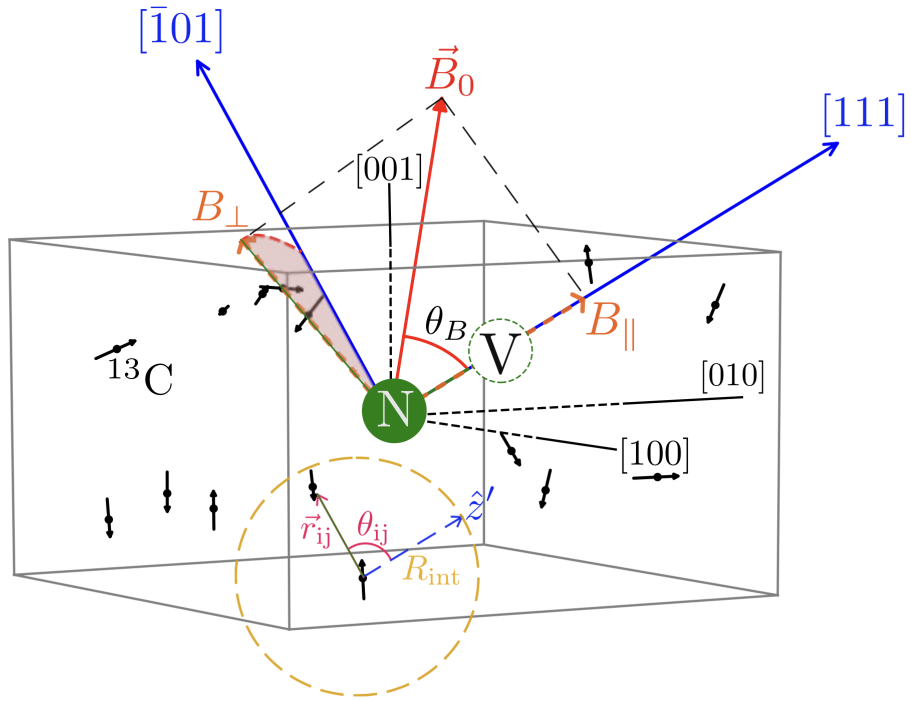

Figure 4.1: Typical single NV-defect aligned in the [111] diamond crystal, the θ_B is the angle between bias magnetic field and [111] direction. Black arrows show spinful ^{13}C isotopes in the environment which contribute to the decoherence of electron spin.

and $\mathbb{D}$ is the dipole-dipole interaction tensor. The spin operators, $\vec{S}$ and $\vec{I}$ are designated for the electron and nuclear spins[2].

It is a common choice to align the bias magnetic field along the NV-axis to split the degeneracy of the $|m_s = \pm 1\rangle$ states. If the bias field is in the orders of $\sim$ 10 mT the non-secular terms in the dipolar hyperfine interaction tensor in H_{int} can be dropped [148, 131]. The dominant hyperfine interaction with the NV-center and the environment mainly consists of the dipolar part of the hyperfine tensor. However, if there exists a proximate (< 1 nm) ^{13}C nuclear site around the vacancy,

[2]The letters with and without subscripts ($\vec{I}_i, \vec{I}, \mathbb{A}_i, \mathbb{A}$) stands for carbon and nitrogen related operators and couplings.

the contribution from the Fermi-contact term of the hyperfine coupling becomes significant. Fortunately, since the typical Fermi-contact interaction radius is too small, there might be only a few of these *near*-vacancy carbon sites and each can be addressed individually by means of dynamical decoupling techniques [7]. Therefore, the main dephasing mechanism for a single NV-center is due to the dipolar-hyperfine interaction type couplings, the fast oscillating terms can be safely dropped.

To calculate the characteristic decoherence time, T_2^*, we consider randomly distributed 1100 ^{13}C spin nuclei over the diamond lattice, which has a typical natural abundance of 1%. Since the single NV-center T_2^* highly depends on the spatial configuration of nuclear spin bath (NSB) [148, 149, 139], to mimic the room temperature dynamics in which the NSB is completely thermalized, we average out 1000 nuclear spin initializations while keeping the spatial positions of the ^{13}C unchanged. Here, I consider NV-sensor which operate at the room temperature and therefore assume that the environment is completely thermalized, *i.e.* $\rho \propto \otimes\hat{\mathbb{I}}^3$. Under these constraints, it is possible to extract the decay factor of single NV-center $\chi(t) = e^{(-t/T_2^*)^p}$ by a home-made generalized Cluster Correlation Expansion (gCCE) [79, 80]. The $\chi(t)$ depend on the physical setting considered for the single NV-center the decay factor has Gaussian profile ($p = 2$) whereas for the ensemble dynamics p becomes 1 [7]. Even though it may seem possible to calculate realistic photoluminescence (PL) streams by employing CCE-based techniques on paper, it is an insufferably hard and unnecessary task for certain CPU clusters. Therefore, after drawing the exponential decay factor from CCE calculations, I prefer to inject the decay factor explicitly into the PL streams calculated.

[3] To mimic the ensemble dynamics one need to seed the nuclear spin positions differently at each realization.

4.2 Interactions in rotating frame of reference

The Hamiltonian terms involved in the typical magnetometry scheme can be written as,

$$H_{\rm NV}/\hbar = DS_z^2 - \gamma_e B_{\rm bias} S_z, \tag{4.5}$$

$$H^i_{\rm MW}/\hbar = -\gamma_e B_x S_x \cos(\omega_{\rm MW} t + \phi_i), \tag{4.6}$$

$$H_{\rm sense}/\hbar = -\gamma_e (B_{\rm calib} + B_{\rm sense}) S_z, \tag{4.7}$$

where we drop the nitrogen degree of freedom and interactions that contribute to the dephasing for simplicity. Here, $H^i_{\rm MW}$ represents the microwave field Hamiltonian applied in the ith stage to flip the NV spin with amplitude B_x and frequency, $\omega_{\rm MW}$[4]. The $H_{\rm sense}$ is the Hamiltonian that contains the sensing field, $B_{\rm sense}$ which is aligned in the quantization axis of the NV-center and can be both DC (time-independent) or AC (time-dependent). Depending on the sensing field type magnetometry pulse scheme can be switched between Ramsey or Hahn echo which are tabulated in Table 4.1 and 4.2. I also add the $B_{\rm calib}$ field which can also be on or off depending on the magnetometry scheme that I am in. Since, $H_{\rm MW}$ has explicit time dependence, it is appropriate to work in a rotating frame of reference which can be achieved by standard mapping,

$$\tilde{H} = U^\dagger_{\rm Rot} H U_{\rm Rot} + i\hbar \dot{U}^\dagger U_{\rm Rot} \tag{4.8}$$

where, $\tilde{H}$ represents the Hamiltonian in the rotating frame, and $U_{\rm Rot} = \exp[-i\omega_{\rm Rot} S_z t]$. In general, H can be splitted into two parts: $H = H_\parallel + H_\perp$, such that $[U_{\rm Rot}, H_\parallel] = 0$, $[U_{\rm Rot}, H_\perp] \neq 0$. If we plug $U_{\rm Rot} = \exp[-i\omega_{\rm Rot} S_z t]$ into Eq. (4.8),

$$\tilde{H} = H_\parallel - \omega_{\rm Rot} S_z + U^\dagger_{\rm Rot} H_\perp U. \tag{4.9}$$

It should be noted that, both $H_{\rm NV}$ and $H_{\rm sense}$ can be lumped into $H_\parallel$, as they both commute with $U_{\rm Rot}$. On the other hand, for the magnetometry stages that the microwave field are turned on, there exists a non-vanishing $H_\perp$ term as $[H^i_{\rm MW}, U_{\rm Rot}] \neq 0$. It is beneficial to calculate, $\tilde{H}^i_{\rm MW} = U^\dagger_{\rm Rot} H^i_{\rm MW} U_{\rm Rot}$,

$$\tilde{H}^i_{\rm MW}/\hbar = -\gamma_e B_x \cos(\omega_{\rm MW} t + \phi_i) U^\dagger_{\rm Rot} S_x U_{\rm Rot}, \tag{4.10}$$

[4]The $H^i_{\rm MW}$ turned on and off depending on the stages shown in Table 4.1 and 4.2 to execute unitary rotations on central spin.

if we set, $\omega_{\mathrm{MW}} = \omega_{\mathrm{Rot}} = \omega$, and use the relation,

$$e^{+i\omega_{\mathrm{Rot}}tS_z} S_x e^{-i\omega_{\mathrm{Rot}}tS_z} = S_x \cos(\omega_{\mathrm{Rot}}t) - S_y \sin(\omega_{\mathrm{Rot}}t), \tag{4.11}$$

then, the microwave Hamiltonian in the rotating frame of reference can be written as,

$$\tilde{H}^i_{\mathrm{MW}}/\hbar = -\frac{\gamma_e B_x}{2}\left[S_x \cos\phi_i + S_y \sin\phi_i\right], \tag{4.12}$$

where we dropped fast-oscillating terms. Therefore, using Eq. 4.9 for a generic ith microwave stage the total Hamiltonian in the rotating frame reduces to,

$$\tilde{H}^i/\hbar = DS_z^2 - \gamma_e B_z S_z - \frac{\gamma_e B_x}{2}\left[S_x \cos\phi_i + S_y \sin\phi_i\right] - wS_z, \tag{4.13}$$

if we tune w resonant with the splitting $D - \gamma_e B_z$, the corresponding matrix representation of the Hamiltonian, $\tilde{H}^i/\hbar$ can be written as,

$$\begin{pmatrix} D - \gamma_e B_z - w & -\frac{\gamma_e B_x}{2\sqrt{2}}(\cos(\phi_i) - i\sin(\phi_i)) & 0 \\ -\frac{\gamma_e B_x}{2\sqrt{2}}(\cos(\phi_i) + i\sin(\phi_i)) & 0 & -\frac{\gamma_e B_x}{2\sqrt{2}}(\cos(\phi_i) - i\sin(\phi_i)) \\ 0 & -\frac{\gamma_e B_x}{2\sqrt{2}}(\cos(\phi_i) + i\sin(\phi_i)) & D + \gamma_e B_z + w \end{pmatrix}. \tag{4.14}$$

This 3×3 matrix is, in fact can be reduced to 2×2 since the $|-1\rangle$ state is highly off-resonant,

$$\tilde{H}^i/\hbar = \begin{pmatrix} 0 & -\frac{\gamma_e B_x}{2\sqrt{2}} e^{-\phi_i} \\ -\frac{\gamma_e B_x}{2\sqrt{2}} e^{+\phi_i} & 0 \end{pmatrix} \tag{4.15}$$

and is equivalent to, $\tilde{H}^i/\hbar = \Omega\vec{\sigma}.\hat{n}/2$, where, the term $\Omega = -\gamma_e B_x/\sqrt{2}$, known as Rabi frequency and $\vec{\sigma} = (\sigma_x, \sigma_y, \sigma_z)$ and $\hat{n} = (\cos(\phi_i), \sin(\phi_i), 0)$. Then, the effective time evolution in the rotating frame of reference, $R^i(t) = \exp\left[-i\tilde{H}^i t/\hbar\right] = \exp\left[-i\frac{\Omega}{2}\vec{\sigma}.\hat{n}t\right]$, so that,

$$R^i(t) = \hat{\mathbb{I}}\cos\left(\frac{\Omega}{2}t\right) - i\vec{\sigma}_n.\hat{n}\sin\left(\frac{\Omega}{2}t\right). \tag{4.16}$$

Let's write the identity operator and spin Pauli matrices for convenience,

$$\begin{aligned}\hat{\mathbb{I}} &= |0\rangle\langle 0| + |1\rangle\langle 0|,\\ \sigma_x &= |1\rangle\langle 0| + |0\rangle\langle 1|,\\ \sigma_y &= i|0\rangle\langle 1| - i|1\rangle\langle 0|,\\ \sigma_z &= |1\rangle\langle 1| - |0\rangle\langle 0|.\end{aligned}$$

Then,

$$\begin{aligned}R^i(t) = &\cos\left(\frac{\Omega}{2}t\right)\left[|0\rangle\langle 0| + |1\rangle\langle 0|\right]\\ &- i\sin\left(\frac{\Omega}{2}t\right)\cos(\phi_i)\left[|1\rangle\langle 0| + |0\rangle\langle 1|\right]\\ &+ \sin\left(\frac{\Omega}{2}t\right)\sin(\phi_i)\left[|1\rangle\langle 1| - |0\rangle\langle 0|\right].\end{aligned}$$

Therefore, $R^i\left(t = \frac{\pi}{2\Omega}\right)$ corresponds to $\pi/2$-pulse so that $\Omega t = \frac{\pi}{2}$ which reduces to,

$$R^i_{\pi/2} = \frac{1}{\sqrt{2}}\left[|0\rangle\langle 0| + |1\rangle\langle 1| - ie^{i\phi_i}|0\rangle\langle 1| - ie^{-i\phi_i}|1\rangle\langle 0|\right] \tag{4.17}$$

On the other hand, $R^i(t = \frac{\pi}{\Omega})$ corresponds to π-pulse and can be written explicitly,

$$R^i_{\pi} = \left[-ie^{i\phi_i}|0\rangle\langle 1| - ie^{-i\phi_i}|1\rangle\langle 0|\right] \tag{4.18}$$

For field interrogation stages in which the NV-center freely evolves under the sensing field in the rotating frame of reference, the sensor Hamiltonian can be written by using Eq. (4.9)

$$\tilde{H}_{\text{free}} = H_{\text{sense}}, \tag{4.19}$$

therefore, the time evolution operator during the free precession,

$$U(t_i, t_f) = \exp\left[\frac{-i}{\hbar}\int_{t_i}^{t_f}\tilde{H}_{\text{free}}(t)dt\right] \tag{4.20}$$

4.3 DC-Magnetometry

For NV-center spin which is prepared in $|0\rangle$, after the pulse sequence $R^{\text{I}}_{\pi/2} - U(0,\tau) - R^{\text{III}}_{\pi/2}$ with field interrogation time τ (see Table 4.1) the final spin state

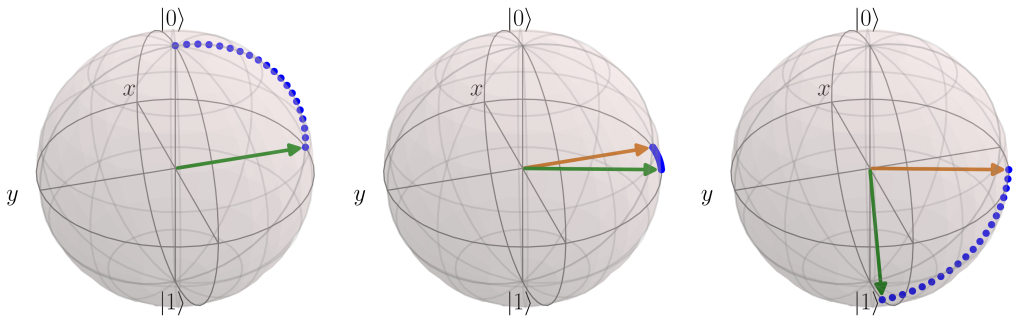

Figure 4.2: Visualisation of Ramsey magnetometry pulse scheme.

at the end of stage-III becomes,

$$|\psi_{\mathrm{III}}\rangle = \frac{1}{2}\left[|0\rangle - ie^{-i(\phi_{\mathrm{I}}+\theta)}|1\rangle - e^{-i(\phi_{\mathrm{I}}+\theta-\phi_{\mathrm{III}})}|0\rangle - ie^{-i\phi_{\mathrm{III}}}|1\rangle\right], \tag{4.21}$$

where, ϕ_{I} and ϕ_{III} are the phases of mw-pulse at corresponding pulse stages, and,

$$\theta = -\gamma_e B_{\mathrm{DC}}\tau, \tag{4.22}$$

is the phase accumulated during the free precession time for the Hamiltonian,

$$H_{\mathrm{sense}}/\hbar = -\gamma_e B_{\mathrm{DC}} S_z, \tag{4.23}$$

where, $B_{\mathrm{DC}} = B_{\mathrm{calib}} + B_{\mathrm{sense}}$.

	Stage I	**Stage II**	**Stage III**
Pulse Applied	$\pi/2$	Free Evolution	$\pi/2$
Hamiltonian (Lab Frame)	$H_{\mathrm{NV}} + H^{\mathrm{I}}_{\mathrm{MW}}$	$H_{\mathrm{NV}} + H_{\mathrm{sense}}$	$H_{\mathrm{NV}} + H^{\mathrm{III}}_{\mathrm{MW}}$
Hamiltonian (Rot Frame)	$\tilde{H}^{\mathrm{I}}$	$\tilde{H}_{\mathrm{free}}$	$\tilde{H}^{\mathrm{III}}$
Unitary Evolution	$R^{\mathrm{I}}_{\pi/2}$	$U(\tau)$	$R^{\mathrm{III}}_{\pi/2}$
State	$\|\psi_{\mathrm{I}}\rangle$	$\|\psi_{\mathrm{II}}\rangle$	$\|\psi_{\mathrm{III}}\rangle$

Table 4.1: Typical Ramsey magnetometry pulse scheme with free evolution time τ, $R^{\mathrm{I}}_{\pi/2} - U(0,\tau) - R^{\mathrm{III}}_{\pi/2}$.

4.3.1 Ramsey optical readout

The optical spin readout contrast is one of the central parameters that determines the minimum detectable field captured by the NV-center along with the decoherence and shot noise. The NV-sensor has a certain optical contrast due to the non-radiative intersystem crossing (ISC) mechanism. The ± 1 states are approximately 30% less luminescent due to ISC transitions when compared to the $|0\rangle$ state which makes the optical spin readout process feasible. However, the average number of photons emitted from $|0\rangle$ and $|\pm 1\rangle$ states per experiment is too small. Therefore, the spin readout process can be associated with the two non-interfering light fields [7]. Thus, let's connect states, $|0\rangle, |1\rangle$ to coherent states $|\beta\rangle, |\alpha\rangle$ respectively, then the photonic $|\psi\rangle_{\text{ph}}$ state can be written as,

$$|\psi\rangle_{\text{ph}} = \frac{1}{2}\left[\left(1 - e^{-i(\phi_I+\theta-\phi_{II})}\right)|0\rangle \otimes |\beta\rangle + \left(-ie^{-i(\phi_I+\theta)} - ie^{-i\phi_{II}}\right)|1\rangle \otimes |\alpha\rangle\right] \tag{4.24}$$

Then, the expectation value for photon number can be calculated as ${}_{\text{ph}}\langle\psi|\hat{N}|\psi\rangle_{\text{ph}}$, where $\hat{N} = \mathbb{I} \otimes (\hat{a}^\dagger\hat{a} + \hat{b}^\dagger\hat{b})$. Here $\hat{a}|\alpha\rangle = \alpha\rangle$ and $\hat{b}|\beta\rangle = \beta|\beta\rangle$ and $\hat{a}|\beta\rangle = 0$ and $\hat{b}|\alpha\rangle = 0$. Let's set $|\alpha|^2 = n_1, |\beta|^2 = n_0$. Then, the expected number of photons can be written as,

$$\begin{aligned}\langle\hat{N}\rangle &= \frac{1}{4}\left(|\beta|^2\left[2 - 2\cos(\Theta)\right] + |\alpha|^2\left[2 + 2\cos(\Theta)\right]\right), \\ &= \frac{n_0 + n_1}{2} + \frac{n_1 - n_0}{2}\cos(\Theta)\end{aligned} \tag{4.25}$$

where, $\Theta = \phi_{\text{I}} - \phi_{\text{II}} + \theta$ is the total phase accumulated. The photon fluctuations, $\Delta N = \sqrt{\langle\hat{N}^2\rangle - \langle\hat{N}\rangle^2}$ can also be calculated, by using the identity $[\hat{a}, \hat{a}^\dagger] = 1$, first calculate,

$$\langle\hat{N}^2\rangle = \frac{n_0(n_0+1)}{2}\left(\cos(\Theta) + 1\right) + \frac{n_1(n_1+1)}{2}\left(\cos(\Theta) - 1\right), \tag{4.26}$$

to arrive at the expression,

$$\Delta N = \sqrt{\frac{n_0 + n_1}{2} + \frac{n_1 - n_0}{2}\cos\Theta + \frac{(n_1 - n_0)^2}{4}(1 - \cos^2(\Theta)}. \tag{4.27}$$

4.3.2 Constructing the estimator for Ramsey magnetometry pulse scheme

For the sake of simplicity, let's assume that the mw-phases in stage-I and stage-III are $\phi_{\mathrm{I,\,III}} = 0$, if we inject the exponential decay factor $\chi(\tau)$ to the expression (4.25), the average number of photons are given by,

$$\langle \hat{N} \rangle = \frac{n_0 + n_1}{2} + \frac{n_1 - n_0}{2} \cos(\Theta)\chi(\tau), \tag{4.28}$$

for a certain value of the Θ, the response of the number of photons is maximized for a small change in the magnetic field. This value can be found by the $\arg\max \left| \frac{\partial}{\partial B_{\mathrm{DC}}} \langle \hat{N} \rangle \right|$. If we calculate the derivative,

$$\frac{\partial}{\partial B_{\mathrm{DC}}} \langle \hat{N} \rangle = \frac{n_1 - n_0}{2} (\gamma_e \tau) \sin(-\gamma_e B_{\mathrm{DC}} \tau)\chi(\tau), \tag{4.29}$$

we can easily observe that when $-\gamma_e B_{\mathrm{DC}} \tau = \pi n/2$, for odd integer values of n, the above expression is maximized. We can assume that at this value of Θ, the response to the magnetic field is almost linear so that the following expression is valid,

$$\frac{\delta B_{\mathrm{DC}}}{\delta \langle \hat{N} \rangle} \approx \frac{1}{\left| \frac{\partial \langle \hat{N} \rangle}{\partial B_{\mathrm{DC}}} \right|_{\mathrm{max}}} \tag{4.30}$$

where, $\delta B_{\mathrm{DC}} = B_{\mathrm{sense}} = (B_{\mathrm{sense}} + B_{\mathrm{calib}}) - B_{\mathrm{calib}}$ is the shift in the magnetic field, similarly, $\delta N = \langle \hat{N} \rangle_{\mathrm{sense\,+\,calib}} - \langle \hat{N} \rangle_{\mathrm{calib}}$, is the change in the average number of photons when there is a sensing field. By modifying the equation 4.30, it is possible to construct the estimator for the sensing field,

$$B_{\mathrm{sense}} = -\frac{\cos(-\gamma_e B_{\mathrm{calib}} \tau)}{\gamma_e \tau}. \tag{4.31}$$

	Stage I	**Stage II**	**Stage III**	**Stage IV**	**Stage V**
PA	$\pi/2$	Free Evolution	π	Free Evolution	$\pi/2$
HL	$H_{\rm NV}+H_{\rm MW}^{\rm I}$	$H_{\rm NV}+H_{\rm sense}$	$H_{\rm NV}+H_{\rm MW}^{\rm III}$	$H_{\rm NV}+H_{\rm sense}$	$H_{\rm NV}+H_{\rm MW}^{\rm V}$
HR	$\tilde{H}^{\rm I}$	$\tilde{H}_{\rm free}$	$\tilde{H}^{\rm III}$	$\tilde{H}_{\rm free}$	$\tilde{H}^{\rm V}$
UE	$R_{\pi/2}^{\rm I}$	$U(0,\tau)$	$R_{\pi}^{\rm III}$	$U(\tau,2\tau)$	$R_{\pi/2}^{\rm V}$
S	$\|\psi_{\rm I}\rangle$	$\|\psi_{\rm II}\rangle$	$\|\psi_{\rm III}\rangle$	$\|\psi_{\rm IV}\rangle$	$\|\psi_{\rm V}\rangle$

Table 4.2: Hahn echo magnetometry pulse scheme with free evolution time τ, $R_{\pi/2}^{\rm I} - U(0,\tau) - R_{\pi}^{\rm III} - U(\tau,2\tau) - R_{\pi/2}^{\rm V}$. PA: pulse applied, HL: Hamiltonian in the lab frame, HR: Hamiltonian in the rotating frame, UE: Unitary evolution, S: sensor state right after the stage.

4.4 AC-Magnetometry

For NV-center initialized in $|\psi\rangle = |0\rangle$, the final state right after the stage-V can be written as

$$\begin{aligned}|\psi_{\rm V}\rangle =& \frac{1}{2}\left(-e^{-i(\phi_{\rm I}-\phi_{\rm III}+\theta(\tau,0))} - e^{-i(\phi_{\rm III}-\phi_{\rm V}+\theta(2\tau,\tau))}\right)|0\rangle \\ &+ \left(-ie^{-i(\phi_{\rm III}+\theta(2\tau,\tau))} + ie^{-i(\phi_{\rm I}-\phi_{\rm III}+\phi_{\rm V}+\theta(\tau,0))}\right)|1\rangle],\end{aligned}$$

where, ϕ_i is the phase of the ith microwave-field given in Eq.(4.6). The $\theta(0,\tau)$ and $\theta(\tau,2\tau)$ are accumulated phases during the stage-II and stage-IV, respectively (these stages tabulated in 4.2) and can be written explicitly as,

$$\theta(0,\tau) = \frac{\gamma_e B_{\rm AC}}{\omega_{\rm AC}}\left[\cos(\omega_{\rm AC}\tau) - 1\right], \tag{4.32}$$

$$\theta(\tau,2\tau) = \frac{\gamma_e B_{\rm AC}}{\omega_{\rm AC}}\left[\cos(\omega_{\rm AC}2\tau) - \cos(\omega_{\rm AC}\tau)\right], \tag{4.33}$$

for the sensing field Hamiltonian,

$$H_{\rm sense} = -\gamma_e B_{\rm AC} S_z \sin(\omega_{\rm AC} t). \tag{4.34}$$

4.4.1 Hahn echo optical readout

To mimic the optical spin readout process let's connect the states $|0\rangle$ and $|1\rangle$ to coherent light states [7], so that,

$$|\psi\rangle_{\text{ph}} = \frac{1}{2}[\left(-e^{-i(\phi_{\text{I}}-\phi_{\text{III}}+\theta(\tau,0))} - e^{-i(\phi_{\text{III}}-\phi_{\text{V}}+\theta(\tau,2\tau))}\right)|0\rangle \otimes |\beta\rangle + \left(-ie^{-i(\phi_{\text{III}}+\theta(\tau,2\tau))} + ie^{-i(\phi_{\text{I}}-\phi_{\text{III}}+\phi_{\text{V}}+\theta(\tau,0))}\right)|1\rangle \otimes |\alpha\rangle] \tag{4.35}$$

Then the expectation value for photon number can be calculated as ${}_{\text{ph}}\langle\psi|\hat{N}|\psi\rangle_{\text{ph}}$, where $\hat{N} = \mathbb{I} \otimes (\hat{a}^\dagger\hat{a} + \hat{b}^\dagger\hat{b})$. Here $\hat{a}|\alpha\rangle = \alpha\rangle$ and $\hat{b}|\beta\rangle = \beta|\beta\rangle$ and $\hat{a}|\beta\rangle = 0$ and $\hat{b}|\alpha\rangle = 0$. If we set the $|\alpha|^2 = n_1, |\beta|^2 = n_0$, the expected value for the photon number yields,

$$\langle\hat{N}\rangle = \frac{n_0 + n_1}{2} + \frac{n_0 - n_1}{2}\cos(\Theta), \tag{4.36}$$

where Θ is the total phase accumulated,

$$\Theta = \phi_{\text{I}} - 2\phi_{\text{III}} + \phi_{\text{V}} + \theta(\tau, 0) - \theta(2\tau, \tau). \tag{4.37}$$

Similar to the Ramsey magnetometry, there is an associated photon fluctuations $\Delta N = \sqrt{\langle\hat{N}^2\rangle - \langle\hat{N}\rangle^2}$, which limits the sensitivity.

4.4.2 Constructing the estimator for Hahn echo magnetometry pulse scheme

For simplicity let's set $\phi_{\text{I}} = 0$ and $\phi_{\text{III}} = 0$, so that we only sweep ϕ_{V} to collect PL data. Then, the accumulated phase reduces to $\Theta = \phi_{\text{V}} + \theta(\tau, 0) - \theta(2\tau, \tau)$. Furthermore, if we adjust interpulse duration time to be $\tau = 1/2f_{\text{AC}}$ to maximize the phase accumulated due to the AC-field the phases become,

$$\theta(0, \tau) = \frac{-2\gamma_e B_{\text{AC}}\tau}{\pi} \tag{4.38}$$

$$\theta(\tau, 2\tau) = \frac{2\gamma_e B_{\text{AC}}\tau}{\pi} \tag{4.39}$$

Thus, the total phase accumulated due to the sensing field can be written explicitly,

$$\Theta_B = \phi_{\text{V}} - \frac{4\gamma_e B_{\text{AC}}\tau}{\pi}, \tag{4.40}$$

so that, if we introduce the decay factor due to decoherence to the $\langle N\rangle_B$, it becomes,

$$\langle N\rangle_B = n_{\text{ave}} + \frac{n_0 - n_1}{2}\cos(\Theta_B)e^{-\chi(t)}. \tag{4.41}$$

Let's find out for which value of Θ_B the expression $\left|\frac{\partial}{\partial B_{AC}}\langle N\rangle_B\right|$ is maximized,

$$\left|\frac{\partial}{\partial B_{\text{AC}}}\langle N\rangle_B\right| = \frac{n_0 - n_1}{2}\frac{4\gamma_e\tau}{\pi}\sin(\Theta_B)e^{-\chi(t)}, \tag{4.42}$$

from the equation above it can be clearly seen that the expression $\left|\frac{\partial}{\partial B_{AC}}\langle N\rangle_B\right|$ is maximized at $\phi_{\text{V}} - \frac{4\gamma_e B_{\text{AC}}\tau}{\phi} = \frac{n\pi}{2}$ where n is an odd integer. Therefore the shift in the PL due to field amplitude B_{AC} can be written approximately as,

$$\frac{\delta B_{\text{AC}}}{\delta\langle N\rangle} = \frac{1}{\partial N/\partial B_{\text{AC}}}, \tag{4.43}$$

it is important to note that here, $\delta B_{\text{AC}} = B_{\text{AC}} - 0$, and $\delta\langle N\rangle = \langle N\rangle_B - \langle N\rangle_0$, and $\langle N\rangle_B$ is the PL collected in the presence of B_{AC} , whereas $\langle N\rangle_0$ is the PL collected when there is no sensing field. Therefore shift in the magnetic field can be approximately written as,

$$B_{\text{AC}} = \frac{\langle N\rangle_B - \langle N\rangle_0}{\frac{n_0 - n_1}{2}\frac{4\gamma_e\tau}{\pi}e^{-\chi(t)}}, \tag{4.44}$$

when the condition $\Theta_B = \frac{n\pi}{2}$ is satisfied the expression above reduces to,

$$B_{\text{AC}} = \frac{-\pi\cos(\theta_{\text{V}})}{4\gamma_e\tau}. \tag{4.45}$$

Chapter 5

Wavelet-based DC-field magnetometry with a single NV-center in diamond

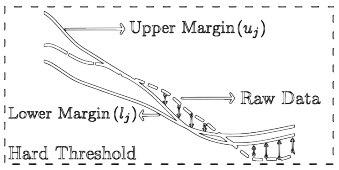

Be precise. A lack of precision is dangerous when the margin of error is small.
— Donald Rumsfeld

This chapter adapted from the preprint [150].

In this chapter, I introduce a Template Margin Thresholding (TMT) method to combat with the photon shot noise (PSN). The approach utilizes a wavelet-based *shrinkage* method tailored specifically to the PSN yet adaptable to other noise sources if needed. TMT is a powerful technique as it provides *on*-resonant filtering which is a thing that frequency-based filters inevitably fail to accomplish. I also show some *assets* and *liabilities* of TMT filtering in Ramsey magnetometry of DC fields.

5.1 Parameter settings

For the DC-field sensing scheme, it is possible to employ the framework prescribed in Table 4.1. Obtain a single data point along the PL time series requires the execution of the following steps:

1. Calculate the transition (survival) probability of the state, $|\psi_{\text{III}}\rangle$ given in Eq. (4.21), by projecting it onto $|1\rangle$ ($|0\rangle$) for a specific free evolution time τ[1]. That is,
$$p(\tau) = |\langle 1|\psi_{\text{III}}(\tau)\rangle|^2 = 1 - |\langle 0|\psi_{\text{III}}(\tau)\rangle|^2 \tag{5.1}$$

2. According the to this $p(\tau)$, project the superposition state, $|\psi_{\text{III}}(\tau)\rangle$ on to either $|0\rangle$ or $|1\rangle$, by means of Bernoulli process [33].

3. Depending on the outcome of Step 2, draw a random sample from Poisson distribution[2],
$$P(k, n_i) = \frac{n_i^k e^{-n_i}}{k!}, \tag{5.2}$$
where k is the number of photons, and n_i is the average number of photons emitted from the state i. Therefore, $P(k, n_1)$ for example can be read as, *"Probability of observing k photons from the spin state* $|1\rangle$*."*

4. Record the sample drawn, and repeat the Steps 1.-4. M times.

While executing these steps for every single free evolution time, τ for some PL interval, $[t_i, t_f]$ to obtain PL-time series we employ three fields. The first field is the bias field (see Eqs. (4.2 - 4.4)), $B_0 = 40$ mT is to split the degenerate energy levels $|\pm 1\rangle$. The second field employed is the $B_{\text{calib}} = 100$ μT which both designates the number of the fringes in the PL stream and extracts a reasonable TMT-filter order that can be used when there is a sensing field. The third field used is the sensing field, B_{sense}, which I aim to measure. Throughout this chapter,

[1]Similarly, For AC-magnetometry scheme a similar state vector ($|\psi_V\rangle$) can be obtained as well (See Sec. 4.4)

[2]Since the average number of photons emitted per experiment is a low number, it is safe to consider $k = 1$.

I set this quantity to 0.5 μT to be able to assess the performance of the TMT filter. Therefore, we assume that, $B_{\text{sense}} \ll B_{\text{calib}} \ll B_0$.

Moreover, I set the optical readout contrast,

$$C = \frac{n_0 - n_1}{n_0 + n_1}, \tag{5.3}$$

to 0.2143 with the average number of photons observed by the photodetector per repetition, $n_{\text{ave}} = (n_0+n_1)/2 = 0.196$ by relying on the experimental values [151]. I would like to note that since observing a photon from a single experiment is a rare event due to small n_{ave} value, the light fields described in Sec. 4.3.1 and 4.4.1 $|\alpha\rangle, |\beta\rangle$ are not correlated. The typical PL stream is collected for some time duration, $T_I = t_f - t_i$, with some sampling rate, f_{sample}, so that the number of data points in PL time series can be calculated by $T_I f_{\text{sample}}$ with each data point requires M independent repetitions. It is appropriate to define a parameter Mt_f to quantify the integration time as it quantifies the time required to calculate the largest PL data in the stream.

5.2 Template margin thresholding (TMT)

After constructing the PL stream, by following the steps in Sec. 5.1, in the presence of both B_{calib} and B_{sense}, I begin by determining the so-called *template* frequency of PL,

$$R(\omega) = \int_{t_i}^{t_f} N^{\text{raw}}(t)\mathcal{K}(t,\omega)dt, \tag{5.4}$$

where, N^{raw} is the raw PL time series, and, $\mathcal{K}(t,\omega)$, is the template waveform and has a very similar structure with the Eq. (4.28),

$$\mathcal{K}(t,\omega) = \frac{1}{2}\left[1 + \cos(wt)e^{-(t/T_{2*})^p}\right], \tag{5.5}$$

to find the template frequency argument that maximizes the function in Eq. (5.4), as illustrated in Fig 5.1. While calculating the overlaps in Eq. (5.4), the DC offsets are subtracted.

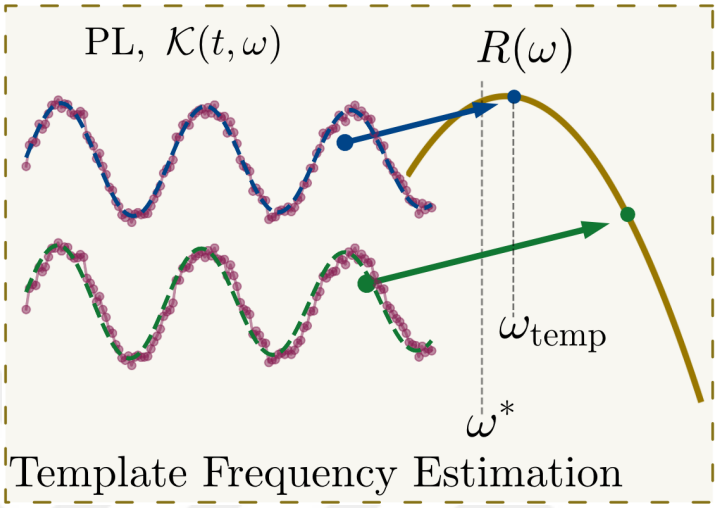

Figure 5.1: Template frequency estimation. The red line represents the PL time series acquired between the interrogation interval $[t_i = 0.97\ \mu\text{s}, t_f = 1.96\ \mu\text{s}]$, with the sampling frequency $f_{\text{sample}} \sim 128$ MHz and $M = 25$K. Blue and green lines show template waveforms tried at different frequencies. The blue line maximizes $R(\omega)$ and is assigned as a template frequency while ω^* is the true value.

Next, by utilizing the characteristic photon fluctuations in Eq. (4.27), it is possible to construct time-dependent upper and lower margins,

$$\mathcal{U}(t) = \mathcal{K}(t, \omega_{\text{temp}}) + 10^{-\beta} \frac{\Delta N}{\sqrt{T_I M f_{\text{sample}}}}, \tag{5.6}$$

$$\mathcal{L}(t) = \mathcal{K}(t, \omega_{\text{temp}}) - 10^{-\beta} \frac{\Delta N}{\sqrt{T_I M f_{\text{sample}}}}, \tag{5.7}$$

where, I call β as the *filter order*, and is introduced to tune the marginal distance. The time budget terms in the denominator are explicitly written since the PSN diminishes by integration time dedicated for sensing protocol [33, 7]. It should be noted that the photon fluctuations in Eq. 4.27 can be written for more complex pulse magnetometry schemes [33] or when multi-frequency components are involved such as when there is a bias field that is slightly misaligned from NV-symmetry axis [152].

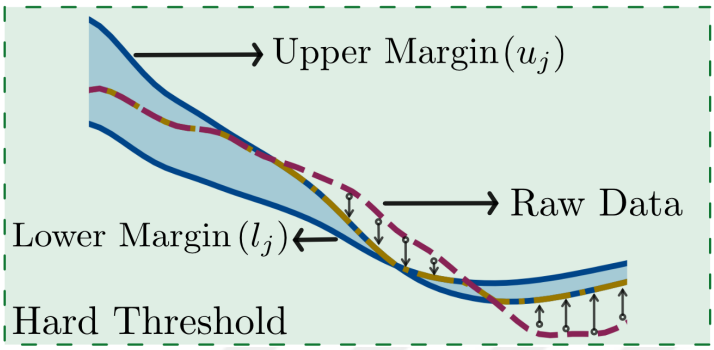

Figure 5.2: *TMT-shrinkage* by means of hard thresholding (Eq. (5.10)). While the blue lines represent the margins, the red dashed line is the raw PL in the specific detail level j, and the yellow line represents the enhanced PL component at this decomposition level.

5.2.1 TMT-shrinkage

By mapping the upper and lower margins in the Eqs (5.6) and (5.7) to the wavelet domain up to the maximum decomposition level, J,

$$\mathrm{UWT}(\mathcal{U}) = [d_0^{\mathcal{U}}, d_1^{\mathcal{U}}, \ldots, d_J^{\mathcal{U}}, c_J^{\mathcal{U}}], \tag{5.8}$$

$$\mathrm{UWT}(\mathcal{L}) = [d_0^{\mathcal{L}}, d_1^{\mathcal{L}}, \ldots, d_J^{\mathcal{L}}, c_J^{\mathcal{L}}], \tag{5.9}$$

for each detail level j, it is possible to construct the margins, $l_{j,k} = \min(d_{j,k}^{\mathcal{U}}, d_{j,k}^{\mathcal{L}})$ and $u_{j,k} = \max(d_{j,k}^{\mathcal{U}}, d_{j,k}^{\mathcal{L}})$ (see Fig 5.2). With a similar approach described in Sec. 2.4, we employ *TMT-shrinkage* such that,

$$R_{j,k}^{\mathrm{hard}} = \begin{cases} d_{j,k}^{\mathrm{raw}}, & l_{j,k} \leq d_{j,k}^{\mathrm{raw}} \leq u_{j,k} \\ u_{j,k}^{\mathcal{K}}, & d_{j,k}^{\mathrm{raw}} > u_{j,k} \\ l_{j,k}^{\mathcal{K}}, & d_{j,k}^{\mathrm{raw}} < l_{j,k} \end{cases}, \tag{5.10}$$

where, R_j^{hard} and d_j^{raw} represent the filtered and raw PL at the jth decomposition level, respectively. I would like to note that, there might exist better shrinkage methods [153], however, for the sake of simplicity I stick to Eq. (5.10). After obtaining *denoised* PL component at each decomposition level, it is possible to recover the time series signal through inverse UWT,

$$N^{\beta} = \mathrm{IUWT}[R_0, R_1, \ldots, R_J, c_J^{\mathrm{raw}}], \tag{5.11}$$

where N^{β} denotes the enhanced PL signal with the filter order β.

5.2.2 TMT flow

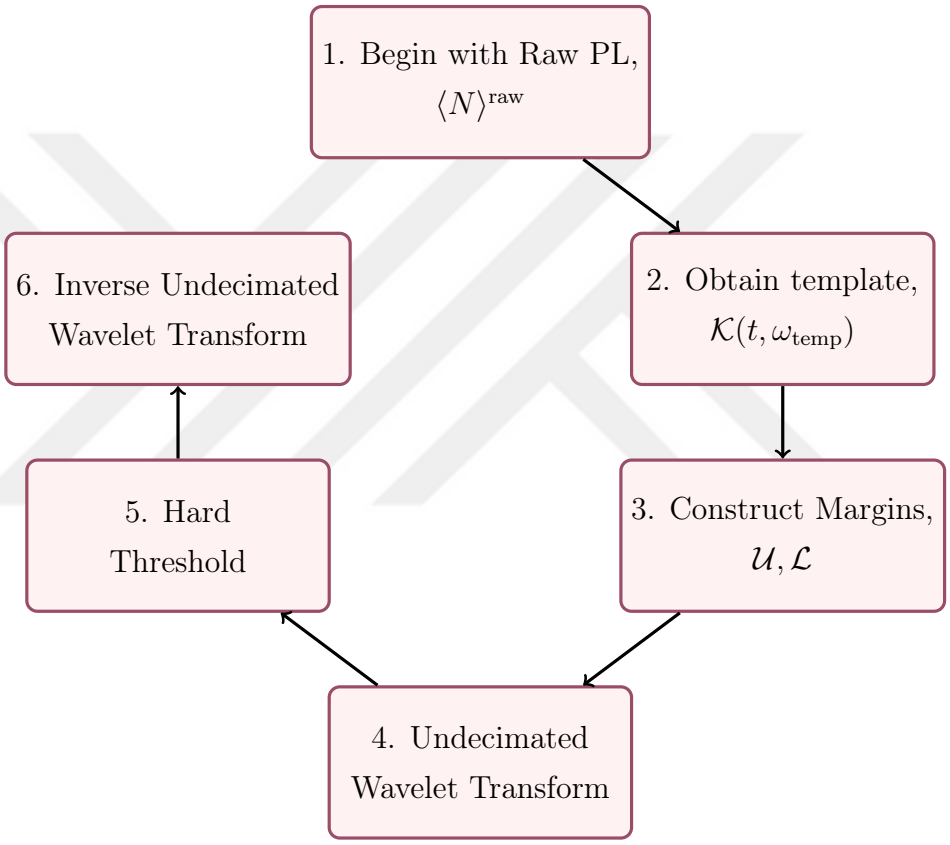

Overall, the TMT method takes advantage of two pieces of information, first, the template waveform that appears for the Ramsey magnetometry pulse scheme, and second, the time-dependent photon shot noise profile. By utilizing this prior knowledge, in the wavelet domain, the noise component of the PL is filtered out. Of course, to retain the time information of noise and the template, I use UWT which is defined in Sec. 2.3.2. The TMT method introduces a distinguished approach when compared to the conventional frequency-based filtering methods which originates from the fact that the conventional frequency filters (lowpass or bandpass) cannot filter the noise at the signal band region to prevent true signal components from attenuation. However, in the wavelet domain, it is possible

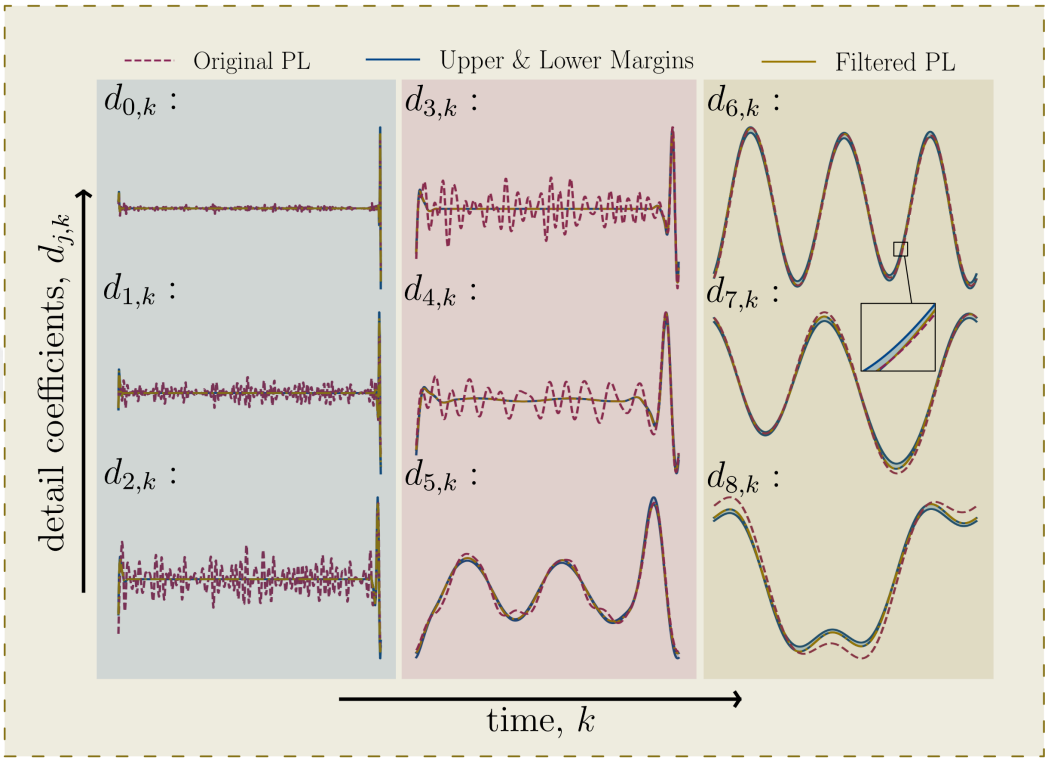

Figure 5.3: Enhancement of PL stream given in Fig. 5.1 by means of hard thresholding. Before the UWT, the PL was interpolated in the time domain so that the Nyquist frequency became 256 MHz. While the horizontal axis shows the discrete time index k, at each decomposition level the vertical axis shows the coefficient amplitude. The inset in $d_{6,k}$ indicates the *on*-resonant PL enhancement.

to enhance a signal of interest both in *near* $(d_{5,k}, d_{7,k})$ and *on* $(d_{6,k})$ resonant frequency bands as illustrated in Fig 5.3. Moreover, the non-stationary behavior of a given signal cannot be handled with *care* as I tried to make clear in Chap. 2.

I should also note that I use biortogonal 6.8 wavelet which is illustrated in Fig. 5.4 as a mother wavelet among the crowded wavelet zoo. The main motivation behind choosing a mother wavelet should be the amount of support at each decomposition level. Especially in the off-resonant band region the *sparse* representation is required to have an effective margin thresholding as shown in Fig 5.3.

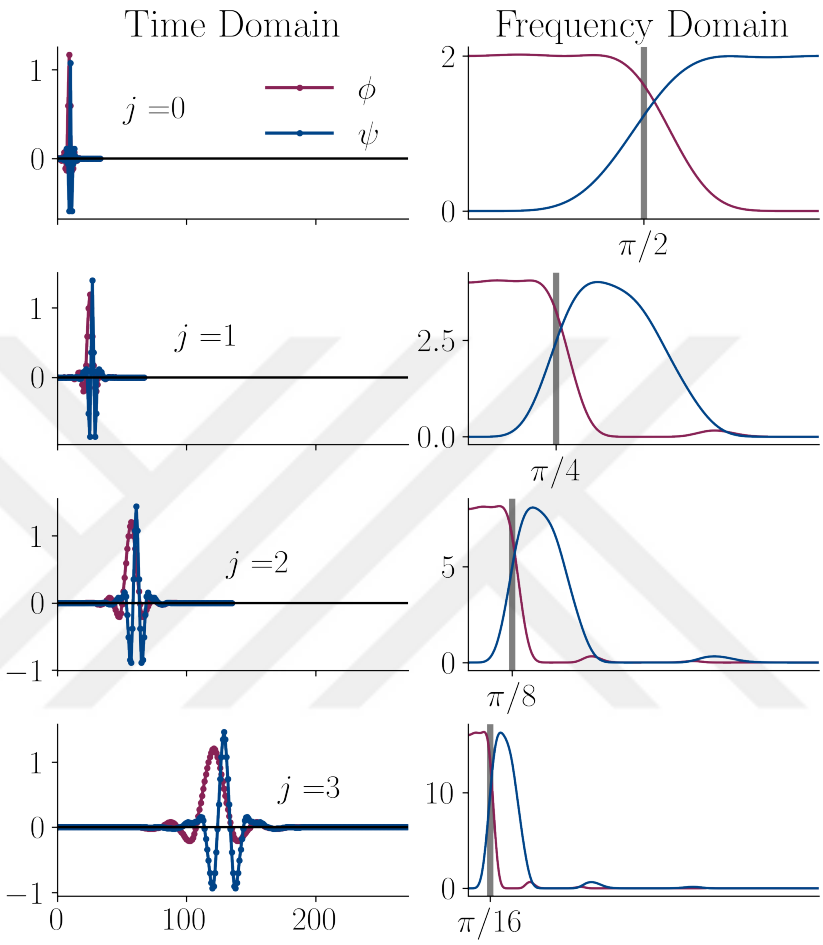

Figure 5.4: Biorthogonal 6.8 wavelet in time and frequency domain representation up to a few detail levels.

5.3 Performance metrics

The points on the PL stream in which we constructed the estimators for the magnetic field in Sec. 4.3.2 and 4.4.2 are known as the slope detection (SD) points. The quantities such as the sensitivity of the NV-center are determined according to the error in the SD points along the PL stream [33, 7]. The average number of photons in the raw PL time series signal is unbiased and a maximum likelihood estimator at SDs. Therefore, the variance (*precision*) is the sole criterion to determine the sensitivity of the NV-center, if the PL stream is not going to be

processed. However, since the TMT method employs a *priori knowledge* (template frequency), it is prone to introduce a bias to the estimation. To encapsulate *precision* along with the *accuracy* of the estimate, the mean squared error (MSE) is a suitable metric [154, 155],

$$\mathrm{MSE}[N^{\beta}(t_q)] = \frac{1}{n_{\mathrm{exp}}} \sum_{i=1}^{n_{\mathrm{exp}}} [N_i^{\beta}(t_q) - N^*(t_q)]^2, \tag{5.12}$$

here, $\mathrm{MSE}[N^{\beta}(t_q)]$ denotes the MSE of TMT-enhanced PL time series with filter order β, $N^*(t_q)$ is the true value for the number of photons at the SD, and the t_q displays the time instance at q^{th} SD point. The n_{exp} is the number of different PL stream realizations that are required for the empirical calculation of MSE. There are $q = 1, \ldots, n_{\mathrm{SD}}$ number of available SDs which are marked by red crosses in the PL time series in the inset of Fig. 5.5 (b). The MSE in Eq. (5.12) can be written by means of bias and variance,

$$\mathrm{MSE}[N^{\beta}(t_q)] = \mathrm{Bias}[N^{\beta}(t_q)]^2 + \mathrm{Var}[N^{\beta}(t_q)], \tag{5.13}$$

where,

$$\mathrm{Bias}[N^{\beta}(t_q)] = \sum_i [N_i^{\beta}(t_q) - N^*(t_q)]/n_{\mathrm{exp}}, \tag{5.14}$$

$$\mathrm{Var}[N^{\beta}(t_q)] = \sum_i [N_i^{\beta}(t_q) - \overline{N_i^{\beta}}(t_q)]^2/n_{\mathrm{exp}}, \tag{5.15}$$

and the overbar represents the sample mean. In the figures shown in Sec. 5.4, I set $n_{\mathrm{exp}} = 2000$. To be able to represent the *goodness* of the estimate with a single value, I also take the average over the fringes for MSE value as, $\mathrm{MSE}[N^{\beta}] = \sum_{q=1}^{n_{\mathrm{SD}}} \mathrm{MSE}[N^{\beta}(t_q)]/n_{\mathrm{SD}}$.

5.4 TMT in action

It is beneficial to discuss the two fundamental limits introduced by TMT-filter. The first limit is the high variance limit in which $\beta \to -\infty$, in this regime TMT-enhanced estimates converge to the raw PL estimates since the marginal distance

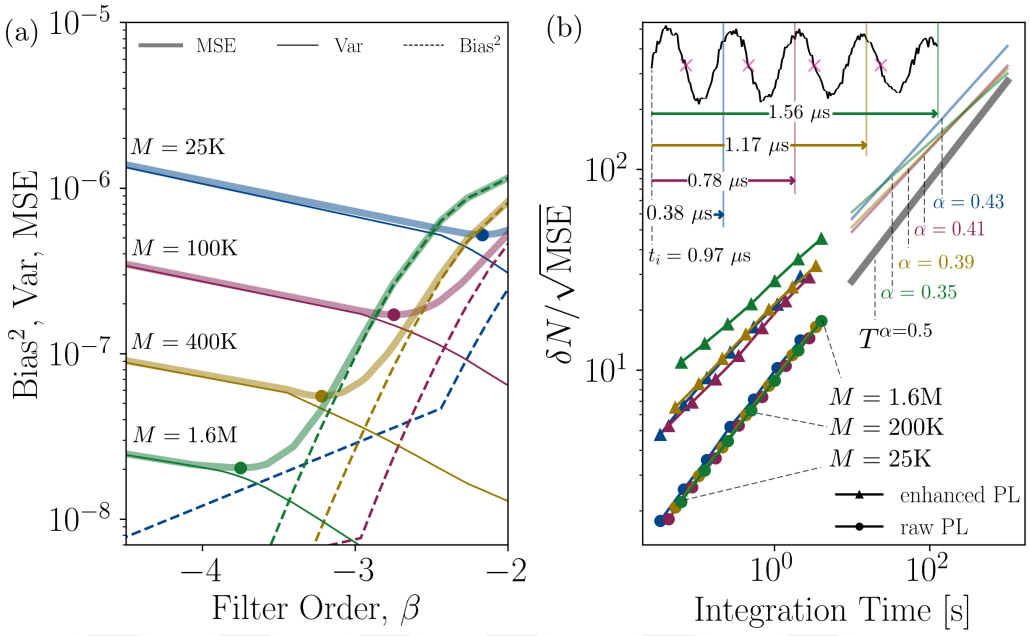

Figure 5.5: For PL time series acquired between [t_i = 0.97 μs, t_f = 2.14 μs] ($n_{\mathrm{SD}} = 3$) with sampling rate, $f_{\mathrm{sample}} \sim 128$ MHz, the bias and variance trade-off is shown as a function of filter order, β. The values that minimize the MSE are marked with dots for each PL stream collected at various M values. (b) The signal-to-noise ratio as a function of total integration time is plotted for the PL time series acquired with different t_f. While the dotted lines represent the raw PL SNRs the triangled lines display the TMT-enhanced PL SNRs. The PL time series acquired for $t_i = 0.97$ μs, to t_f values, 1.36 μs (blue), 1.75 μs (red), 2.14 μs (yellow), 2.53 μs with $f_{\mathrm{sample}} \sim 128$ MHz and each data point obtained at the optimum filter order.

becomes infinitely large and therefore there will be no reassignment of the detail coefficients of the PL streams in the wavelet domain. On the other hand, if I let $\beta \to +\infty$ the marginal distance is going to become infinitely small, and TMT-enhanced PL converges to the initial template function, $\mathcal{K}(t, \omega_{\mathrm{temp}})$ and it showcases the high-bias regime. Overall, there is a bias-variance trade-off that needs to be considered while determining the filter order β. This trade-off can be observed in Fig. 5.5 (a) as the contribution of both bias and variance to the MSE is plotted as a function of filter order employed at different repetition numbers M. It should also be noted that for certain filter orders β_{opt} the MSE values are minimized which are also marked with dots in Fig. 5.5 (a). I would like to refer to

these points as, *optimum* filter orders as they give the maximum signal-to-noise ratios (SNR) for the PL-time series.

I plot SNR values which are defined as the average shift due to the sensing field, divided by the MSE, as a function of the integration time in Fig. 5.5. A typical SNR can be fit to a form $c(MT_I)^{\alpha}$ with respect to budget invested at fixed f_{sample}. Here, I refer to c and α as the prefactor and exponent, respectively. The distinct optimum filter orders, β_{opt}, possess different exponents which are all characteristically below the so-called Standard Quantum Limit (SQL, i.e. $\alpha < 0.5$) due to the bias contribution to the overall MSE. Nevertheless, the overall performance gain is obtained thanks to large prefactors and the suppressed variance. The inferior scaling of enhanced PL time series favors the low-time-budget applications of the TMT method.

5.4.1 Some remarks on sub-SQL scaling of TMT

To be able to understand the inferior scaling characteristics of TMT, let's focus on a single SD point on the PL stream which is constructed over M repetitions. Then, the estimator for $\hat{N}$ can be written as sample mean,

$$\hat{N} = \frac{1}{M}\sum_{i=1}^{M} N_i, \tag{5.16}$$

here, N_i is the number of photons observed in the ith sample. The MSE of the estimation can be written as,

$$\begin{aligned}
\text{MSE}[\hat{N}] &= \text{Var}\left[\hat{N}\right] + \text{Bias}\left[\hat{N}\right]^2, \\
&= \text{Var}\left[\frac{1}{M}\sum_{i=1}^{M} N_i\right] + \text{Bias}\left[\frac{1}{M}\sum_{i=1}^{M} N_i\right]^2, \\
&= \frac{1}{M^2}\text{Var}\left[\sum_{i=1}^{M} N_i\right] + \text{Bias}\left[\frac{1}{M}\sum_{i=1}^{M} N_i\right]^2,
\end{aligned}$$

since, raw PL, the estimation is an unbiased one, and hence MSE reduces to,

$$\sqrt{\text{MSE}} = \frac{1}{M}\sqrt{\sum_{i=1}^{M} \text{Var}[N_i]} = \frac{1}{M}\sqrt{M\sigma_{\text{raw}}^2} = \frac{\sigma_{\text{raw}}}{\sqrt{M}},$$

which corresponds to the standard error, here, we let $\text{Var}[N_i] = \sigma_{\text{raw}}^2$ for $i = 1, \ldots, M$ since we assume that all repetitions have identical properties. Under this condition, we arrive at the SQL scaling ($\sqrt{M}$). For enhanced PL, the standard deviation is smaller than the raw PL's standard deviation and therefore is not the reason behind inferior SQL scaling (i.e. $\sigma_{\text{TMT}} < \sigma_{\text{raw}}$, where σ_{TMT} is the standard deviation for TMT filtered PL SD point.). However, we have a non-vanishing bias contribution to the overall MSE $\epsilon = \text{Bias}\left[\sum_{i=1}^{M} N_i/M\right]$ which can be written in terms of M with some exponent γ, that is, $\epsilon(M) = \epsilon_0 M^{\gamma}$. In this case, the square root of the MSE can be written as,

$$\begin{aligned}\sqrt{\text{MSE}} &= \frac{1}{M}(M\sigma_{\text{TMT}}^2 + \epsilon_0^2 M^{2\gamma})^{1/2}, \\ &= M^{\gamma-1}(M^{1-2\gamma}\sigma_{\text{TMT}}^2 + \epsilon_0^2)^{1/2}. \end{aligned} \tag{5.17}$$

To have an inferior SQL characteristic as indicated in Fig. 5.5 (b), the exponent of the bias term should be somewhere in between $0.5 < \gamma < 1$. For a typical value M which is in general quite large, the expression in Eq. (5.17) practically becomes $M^{\gamma-1}\epsilon_0$, which yields a sub-SQL scaling.

5.4.2 Comparing TMT with frequency-based filters

To benchmark TMT against conventional frequency-based filters, I employ a sixth-order Butterworth lowpass filter, which has a maximally flat frequency response in the passband. To neutralize the phase response of the Butterworth lowpass filter, it is possible to apply forward-backward filtering so that the SD points remain unaffected. Since PL streams are acquired in the rotating frame of reference with calibration field 100 μT, the true PL has a central frequency around 2.8 MHz. With the frequency resolution of 0.28 MHz for the PL time series collected for the interval $[t_i = 0.2\ \mu\text{s}, t_f = 3.7\ \mu\text{s}]$, I set the corner-frequency of the Butterworth filter to be 5 MHz. It should be noted that since the true

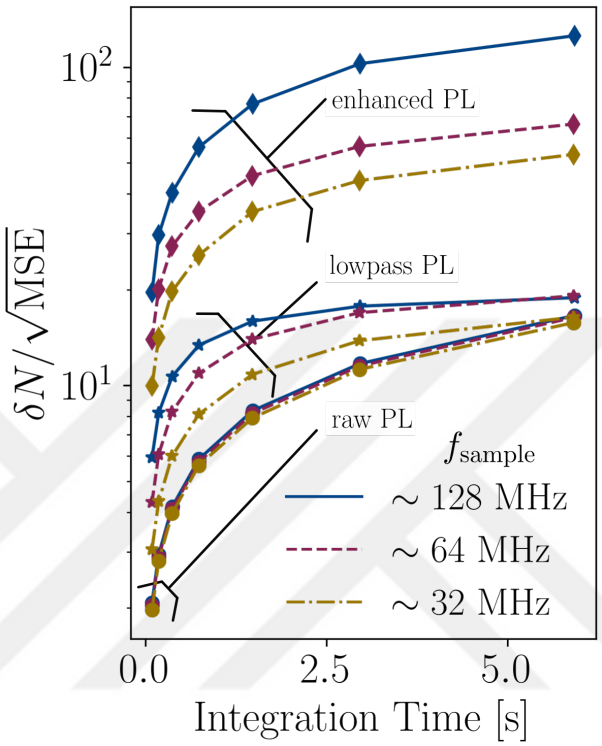

Figure 5.6: SNRs of PL time series acquired at different sampling rates for fixed $T_I = 3.\ \mu$s with ($[t_i = 0.2\ \mu$s, $t_f = 3.7\ \mu$s$]$) which includes nine SD points. While lines with circles and stars represent SNRs of raw and lowpass filtered PL streams, the lines with triangle markers correspond to TMT-enhanced PLs.

signal frequency is not well isolated from the DC wall, it prevents a bandpass filter from being able to operate at a desirably high order.

In Fig. 5.6, I have displayed SNRs of raw, lowpass, and TMT-enhanced PL streams at the slope detection points for a fixed, T_I at various sampling rates. Along the same line from left to right, the number of repetitions M is doubled starting from 25K to 1.6M. It can be observed that while the lowpass filter operates effectively at low M, SNR values at high M start to converge to the raw PL performance, since increasing M practically lowers the shot noise floor in the frequency representation. Moreover, for higher sampling rates the lowpass filtered SNRs improve for the low time budgets as higher frequency components of PSN are resolved and hence can be filtered out. The TMT-enhanced PL streams, on

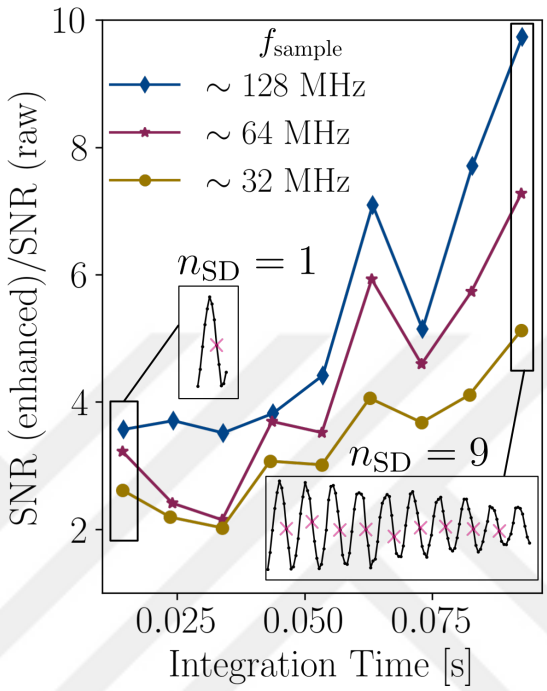

Figure 5.7: For fixed $M = 25$ K the normalized SNRs are demonstrated for increasing PL durations from one SD ($[t_i = 0.2\ \mu$s, $t_f = 0.58\ \mu$s$]$) to 9 SDs ($[t_i = 0.2\ \mu$s, $t_f = 3.7\ \mu$s$]$) as shown by the insets. In each data point along the horizontal axis, the PL time series is prolonged approximately by an amount of 0.38 μs. Each line corresponds to PL SNRs acquired for different sampling rates (While the yellow is collected at $f_{\text{sample}} \sim 32$ MHz, red and blue lines are collet at 64 MHz, and 128 MHz, respectively.). Each data point is obtained for the filter order that minimizes the MSE of the calibration PL time series.

the other hand, perform much better when compared to the conventional lowpass filter. This is mainly because of the fact that with TMT it is possible to do a signal enhancement not only *off*-resonant frequency band (as frequency-based filters do) but also *near*- and *on*-resonant frequency bands. In addition to resolving high-frequency noise components similar to the lowpass filter case, increasing the sampling frequency increases the accuracy of ω_{temp} prediction.

5.4.3 Practical use of TMT-filter

The performance of the TMT-estimate is maximized when operated with the filter order β_{opt} as it is the filter order that minimizes the MSE. However, determining β_{opt} requires the true values for the average number of photons in the PL time series, $N^*(t_q)$ which is an impractical task as it is the parameter we would like to estimate. At this stage, the calibration PL time series becomes handy in determining the optimal filter order when there is a sole calibration field in the measurement. This filter order then can be used when there is an actual sensing field introduced. Even though, this *calibrated* filter order is not guaranteed to be the best option available when there is a sensing field, as long as the time budget parameters are the same, it is expected to be close to this predefined filter order. To support this idea, in Fig 5.7, I optimize the filter orders according to the calibration field and then use them in the sensing. To make TMT-performance improvement more illuminating to the naked eye, SNR of the TMT-filtered PLs are normalized with respect to raw ones (i.e. $\sqrt{\text{MSE}[N^{\text{raw}}]/\text{MSE}[N^{\beta}]}$) at varying sampling frequencies. This time, I increase the PL duration at fixed repetitions $M = 25$ K which improves the performance of the TMT filter.

5.4.4 General Traits

Overall, it seems that long PL streams along with the low repetitions M it is possible to achieve very large performance improvements for each slope detection point available. Especially when the sampling frequency is large (128 MHz) an order of magnitude imporovement can be achieved. It should also be noted that TMT-enhanced PL is an asymptotically *consistent* estimator as $M \to \infty$, $\omega_{\text{temp}} \to \omega^*$ even if it is a biased one. In principle, for finite time budgets, the only barrier that limits the performance of the TMT is the decoherence of the NV-center, since the kernel in Eq. (5.4), prioritizes the early fringes more while determining the template frequency, after some free evolution time, prolonging the PL stream does not contribute to choosing a better template. Therefore, the performance of the TMT method can be boosted further in purified NV-centers

which have decoherence time around 90 μs [156], or T_2^* extended schemes by spin-bath driving [7].

Chapter 6

Recursive Template Margin Thresholding

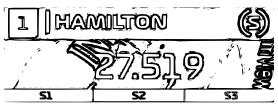

Team Radio: *Ok Lewis, close that gap as much as you can. It's hammer time!*

— Peter Bonnington

Throughout this chapter, I discuss how one can free thyself from the *liabilities* introduced by the standard-TMT filter. Recall that the standard-TMT lost its advantage in high-time budget applications. As elaborated in Sec. 5.4, this originates from the bias contribution of the TMT-enhanced PL estimate causing an inferior SQL scaling. Here, I show that it is possible to keep bias contribution under control by changing the philosophy in establishing the initial template and adjusting the margins *recursively*. Then, I conclude with how this freshly forged approach performs compared to the old friend (standard-TMT).

The original version of the image above has been taken from the source [157].

6.1 Recursive TMT

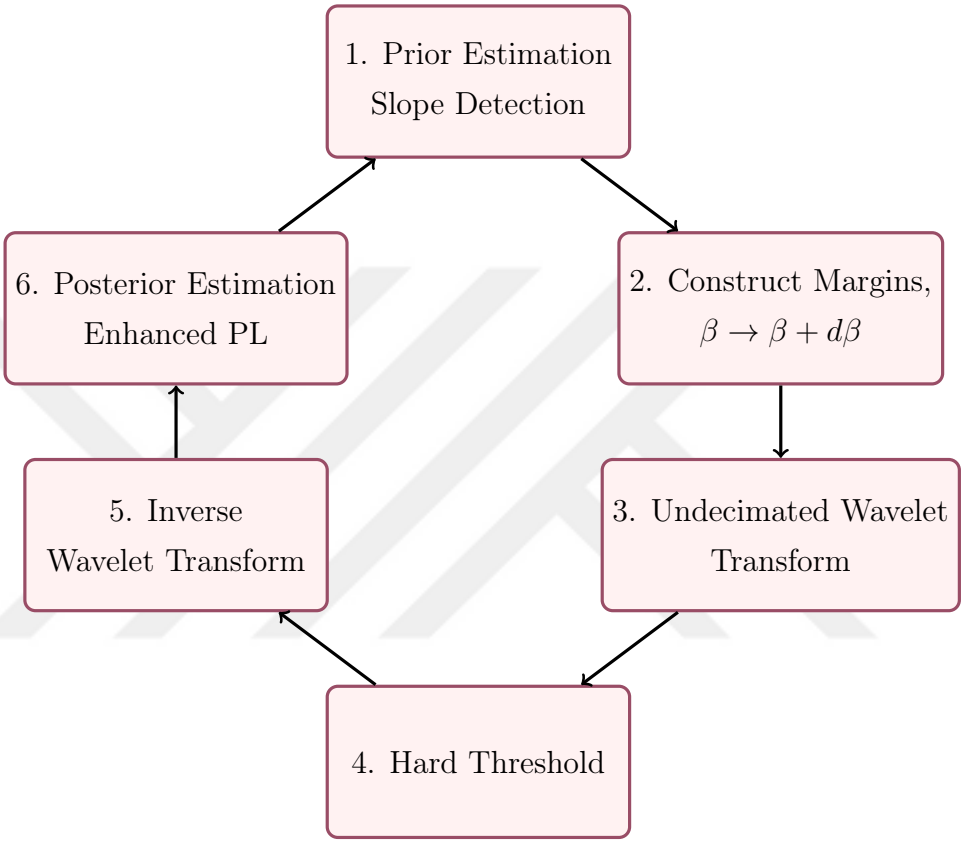

This time, instead of employing the kernel in Eq. (5.4), I begin with the ordinary SD estimation in which the PL response of magnetic field change is maximized. The template obtained from the kernel in standard-TMT introduces a large bias and prevents TMT from operating at a desirably high filter order. To mitigate this, I use the SD point as an initial template as it is a maximum likelihood estimate and hence is an unbiased one. Furthermore, it might be more adaptable to the various waveforms when different sensing protocols are involved. Next, margins, $\mathcal{U}, \mathcal{L}$, are constructed according to this template. After, following the standard procedure in UWT, thresholding, and calculating the inverse UWT, another SD can be made on the enhanced PL series. This posterior measurement can be used as a prior estimate in the next cycle. It is important to note that at each iteration increasing the filter order by a very small amount provides both prevention of bias from blowing up and narrowing the marginal distance

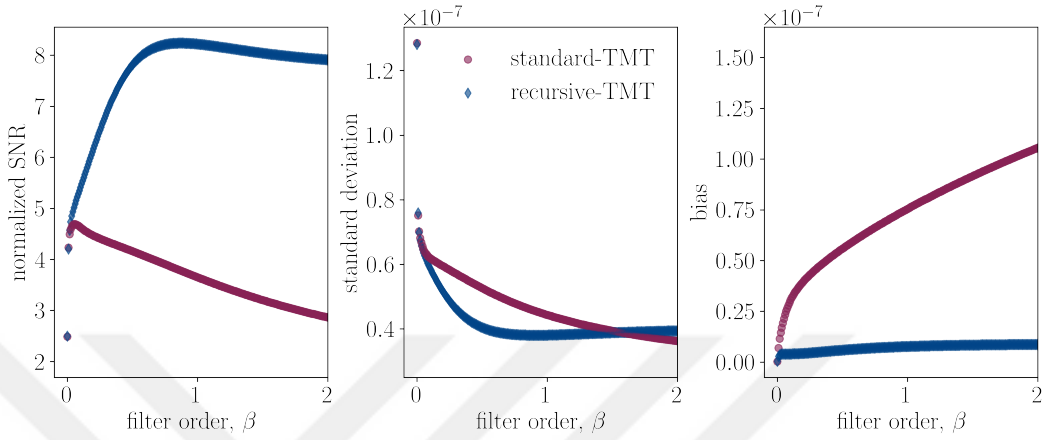

Figure 6.1: Comparision of standard- (red dots) and recursive-TMT (blue diamonds) for PL stream collected as a function of last microwave phase with $B_{\mathrm{AC}} = 9 \times 10^{-7}$, $f_{\mathrm{AC}} = 0.5$ MHz, $f_{\mathrm{sample}} = 80$ rad^{-1}, $M = 100$K. The left, middle, and right panels display normalized SNR, standard deviation, and bias as a function of the filter order employed.

effectively. Repeating this cycle a few times recursively lets us reach an optimum filter order that minimizes the MSE.

6.2 Comparison with standard-TMT

To compare the performance of recursive-TMT with the standard-TMT, I have considered an AC field with a Hahn Echo pulse scheme. The PL stream is acquired by sweeping the last $\pi/2$ pulse phase from 0 to π. In the left panel of Fig. 6.1, I display the normalized SNRs of standard- and recursive-TMT performances. The performance of the TMT method can be further improved by using a recursive approach. It is noteworthy that for the lowest filter order value, the performances of both approaches coincide as it is the very first loop of the recursive-TMT, and the filter order is quite low. In the middle and right pane, the standard deviation and bias contribution to the MSE error are also displayed as a function of filter order, respectively. While the bias drastically increases for standard-TMT for high filter orders, the recursive method keeps the bias contribution essentially

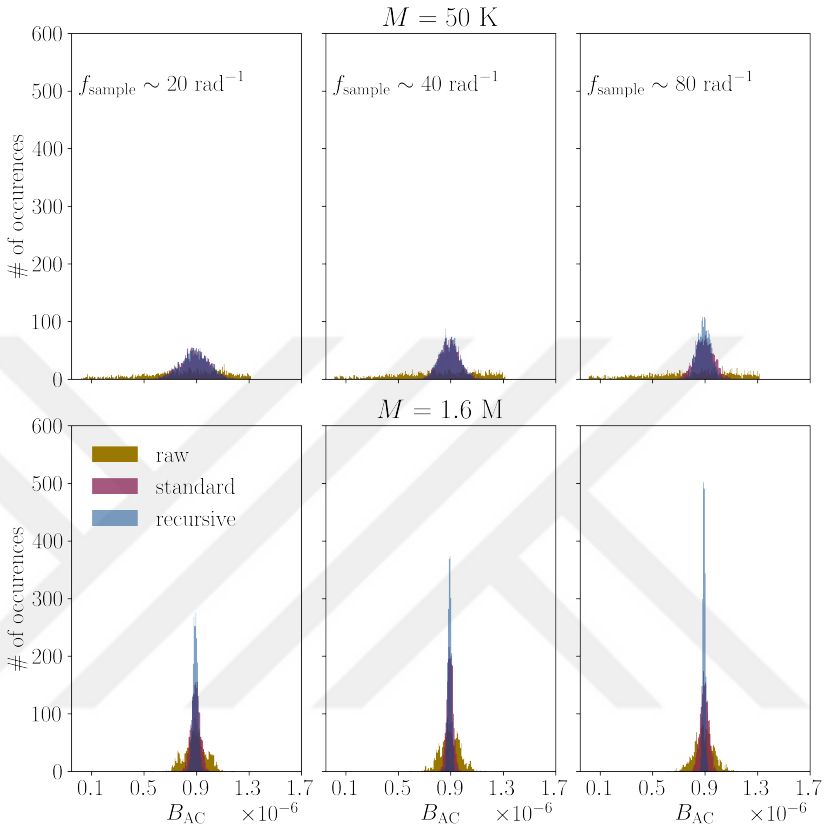

Figure 6.2: Histograms of the estimations drawn from, $n_{\text{exp}} = 2000$, independent PL streams collected as a function of last mw phase with $B_{\text{AC}} = 9 \times 10^{-7}$, $f_{\text{AC}} = 0.5$ MHz at different sampling rates. Upper ($M = 50$ K) and lower ($M = 1.6$ M) panels display the realizations at different repetitions. Yellow, red, and blue bars represent the estimations obtained from raw, standard, and recursive enhanced TMT data.

under control.

In Fig. 6.2, the histograms regarding the magnetic field estimations are displayed for $n_{\text{exp}} = 2000$ independent realizations of PL streams obtained in low ($M = 50$ K) and high time budget regime ($M = 1.6$ M). Increasing the sampling rate directly reflects the performance of the recursive-TMT filter as expected. The performance improvement persists for recursive-TMT at high-budget applications, while standard-TMT shows *signs of wear and tear*. Therefore, preventing

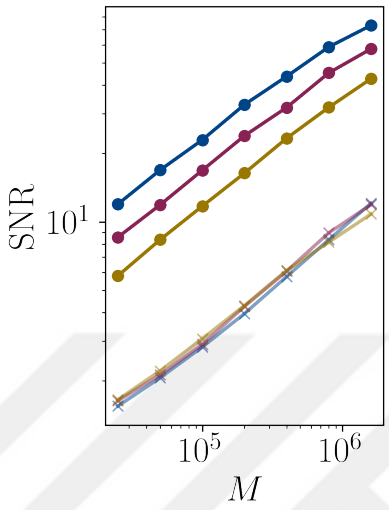

Figure 6.3: Scaling of raw and recursive-TMT enhanced PL streams as a function of number of repetitions at various sampling rates, with $B_{\mathrm{AC}} = 9 \times 10^{-7}$, $f_{\mathrm{AC}} = 0.5$ MHz, $f_{\mathrm{sample}} \sim 20$ rad^{-1} (yellow), $f_{\mathrm{sample}} \sim 40$ rad^{-1} (red), $f_{\mathrm{sample}} \sim 80$ rad^{-1} (blue), while crosses corresponds to raw PL dots represent recursive-TMT enhanced PL streams.

bias from rapid escalation by the recursive approach allows us to operate practically with SQL scaling as illustrated in Fig. 6.3.

Chapter 7

Conclusion and outlook

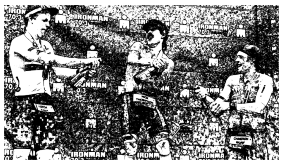

Climb the mountain so you can see the world,
not so the world can see you.
— David McCulloug Jr.

Finally, let me briefly underline the things that I came to realize during my PhD expedition:

First, continuous wavelet-based approaches can be utilized to extract information about the spatial configuration of both single (stripe) and neighboring spin sites (forming beat patterns) in CS confined in a semiconductor host material provided that the dominant hyperfine coupling is of the Fermi-contact type. If the reservoir is dilute, the displacement vector that connects neighboring spins can be distinguishable to the eye that resides within a few neighboring shells.

Next, PSN is one of the fundamental constraints that limit the sensitivity of the NV-center. Fortunately, it is possible to tailor a wavelet-based technique

The original version of the image above has been taken from the source [158].

(template margin thresholding) to suppress it. Unlike the frequency-based conventional filter, it allows to do *on-resonant* filtering without attenuating the true signal. The method relies on the prior template and utilizes this information in the wavelet basis in which PL of interest is represented in separate chunks of frequency bands. Unfortunately, the TMT method loses its *unfair* advantage when it comes to the high-time budget applications, due to the bias contribution to the overall MSE which is commonly referred as inferior SQL scaling. Finally, I managed to show that by changing the philosophy in determining the *template* and updating the TMT filter order in small steps it is possible to reclaim the SQL scaling.

7.1 Future work

TMT method can be adapted to different measurement protocols such as optically detected nuclear magnetic resonance other than Ramsey or Hahn Echo magnetometry. Moreover, the settings in which multiple parameters are simultaneously unknown such as magnitude and frequency require a joint estimation which might be an interesting one that TMT can operate. In all of the scenarios described above, the adaptation of TMT to the ensemble sensing is crucial in which various non-uniformities are involved. Last, but not least, hopefully I will deploy the TMT as a Python package (pytmt) for use by general public and generalize for user defined margins to get rid of case-specific noises that may originate from the technical equipment.

Bibliography

[1] E. Britannica, "Mount everest," 2024. Accessed: 2024-07-22.

[2] M. Driscoll, "Book of books," Aug. 2023. Publisher: University of Copenhagen.

[3] D. D. Awschalom, L. C. Bassett, A. S. Dzurak, E. L. Hu, and J. R. Petta, "Quantum Spintronics: Engineering and Manipulating Atom-Like Spins in Semiconductors," *Science*, vol. 339, pp. 1174–1179, Mar. 2013. Publisher: American Association for the Advancement of Science.

[4] A. Chatterjee, P. Stevenson, S. De Franceschi, A. Morello, N. P. de Leon, and F. Kuemmeth, "Semiconductor qubits in practice," *Nature Reviews Physics*, vol. 3, pp. 157–177, Mar. 2021. Publisher: Nature Publishing Group.

[5] G. Burkard, T. D. Ladd, A. Pan, J. M. Nichol, and J. R. Petta, "Semiconductor spin qubits," *Reviews of Modern Physics*, vol. 95, p. 025003, June 2023. Publisher: American Physical Society.

[6] C. L. Degen, "Scanning magnetic field microscope with a diamond single-spin sensor," *Applied Physics Letters*, vol. 92, p. 243111, 06 2008.

[7] J. F. Barry, J. M. Schloss, E. Bauch, M. J. Turner, C. A. Hart, L. M. Pham, and R. L. Walsworth, "Sensitivity optimization for nv-diamond magnetometry," *Rev. Mod. Phys.*, vol. 92, p. 015004, Mar 2020.

[8] J. Cai, A. Retzker, F. Jelezko, and M. B. Plenio, "A large-scale quantum simulator on a diamond surface at room temperature," *Nature Physics*, vol. 9, pp. 168–173, Mar. 2013. Publisher: Nature Publishing Group.

[9] G. Wolfowicz, A. M. Tyryshkin, R. E. George, H. Riemann, N. V. Abrosimov, P. Becker, H.-J. Pohl, M. L. W. Thewalt, S. A. Lyon, and J. J. L. Morton, "Atomic clock transitions in silicon-based spin qubits," *Nature Nanotechnology*, vol. 8, pp. 561–564, Aug. 2013. Publisher: Nature Publishing Group.

[10] S. Choi, J. Choi, R. Landig, G. Kucsko, H. Zhou, J. Isoya, F. Jelezko, S. Onoda, H. Sumiya, V. Khemani, C. von Keyserlingk, N. Y. Yao, E. Demler, and M. D. Lukin, "Observation of discrete time-crystalline order in a disordered dipolar many-body system," *Nature*, vol. 543, pp. 221–225, Mar. 2017. Publisher: Nature Publishing Group.

[11] D. P. DiVincenzo, "The Physical Implementation of Quantum Computation," *Fortschritte der Physik*, vol. 48, no. 9-11, pp. 771–783, 2000. _eprint: https://onlinelibrary.wiley.com/doi/pdf/10.1002/1521-3978%28200009%2948%3A9/11%3C771%3A%3AAID-PROP771%3E3.0.CO%3B2-E.

[12] M. H. Abobeih, J. Cramer, M. A. Bakker, N. Kalb, M. Markham, D. J. Twitchen, and T. H. Taminiau, "One-second coherence for a single electron spin coupled to a multi-qubit nuclear-spin environment," *Nature Communications*, vol. 9, no. 1, p. 2552, 2018.

[13] A. M. Tyryshkin, S. A. Lyon, A. V. Astashkin, and A. M. Raitsimring, "Electron spin relaxation times of phosphorus donors in silicon," *Physical Review B*, vol. 68, p. 193207, Nov. 2003.

[14] X. Rong, J. Geng, F. Shi, Y. Liu, K. Xu, W. Ma, F. Kong, Z. Jiang, Y. Wu, and J. Du, "Experimental fault-tolerant universal quantum gates with solid-state spins under ambient conditions," *Nature Communications*, vol. 6, p. 8748, Nov. 2015. Publisher: Nature Publishing Group.

[15] M. T. Mądzik, S. Asaad, A. Youssry, B. Joecker, K. M. Rudinger, E. Nielsen, K. C. Young, T. J. Proctor, A. D. Baczewski, A. Laucht, V. Schmitt, F. E. Hudson, K. M. Itoh, A. M. Jakob, B. C. Johnson, D. N. Jamieson, A. S. Dzurak, C. Ferrie, R. Blume-Kohout, and A. Morello, "Precision tomography of a three-qubit donor quantum processor in silicon," *Nature*, vol. 601, pp. 348–353, Jan. 2022. Publisher: Nature Publishing Group.

[16] T. Xie, Z. Zhao, S. Xu, X. Kong, Z. Yang, M. Wang, Y. Wang, F. Shi, and J. Du, "99.92-fidelity cnot gates in solids by noise filtering," *Phys. Rev. Lett.*, vol. 130, p. 030601, Jan 2023.

[17] M. Gaudin, "Diagonalisation d'une classe d'hamiltoniens de spin," *Journal de Physique*, vol. 37, pp. 1087–1098, Oct. 1976. Publisher: Société Française de Physique.

[18] I. A. Merkulov, A. L. Efros, and M. Rosen, "Electron spin relaxation by nuclei in semiconductor quantum dots," *Physical Review B*, vol. 65, p. 205309, Apr. 2002. Publisher: American Physical Society.

[19] A. V. Khaetskii, D. Loss, and L. Glazman, "Electron Spin Decoherence in Quantum Dots due to Interaction with Nuclei," *Physical Review Letters*, vol. 88, p. 186802, Apr. 2002. Publisher: American Physical Society.

[20] W. A. Coish and D. Loss, "Hyperfine interaction in a quantum dot: Non-markovian electron spin dynamics," *Phys. Rev. B*, vol. 70, p. 195340, Nov 2004.

[21] L. Cywiński, W. M. Witzel, and S. Das Sarma, "Pure quantum dephasing of a solid-state electron spin qubit in a large nuclear spin bath coupled by long-range hyperfine-mediated interactions," *Physical Review B*, vol. 79, p. 245314, June 2009. Publisher: American Physical Society.

[22] W.-L. Ma, G. Wolfowicz, N. Zhao, S.-S. Li, J. J. L. Morton, and R.-B. Liu, "Uncovering many-body correlations in nanoscale nuclear spin baths by central spin decoherence," *Nature Communications*, vol. 5, p. 4822, Sept. 2014. Publisher: Nature Publishing Group.

[23] R. Hanson, V. V. Dobrovitski, A. E. Feiguin, O. Gywat, and D. D. Awschalom, "Coherent Dynamics of a Single Spin Interacting with an Adjustable Spin Bath," *Science*, vol. 320, pp. 352–355, Apr. 2008. Publisher: American Association for the Advancement of Science.

[24] B. Urbaszek, X. Marie, T. Amand, O. Krebs, P. Voisin, P. Maletinsky, A. Högele, and A. Imamoglu, "Nuclear spin physics in quantum dots: An optical investigation," *Reviews of Modern Physics*, vol. 85, pp. 79–133, Jan. 2013. Publisher: American Physical Society.

[25] J. R. Klauder and P. W. Anderson, "Spectral Diffusion Decay in Spin Resonance Experiments," *Physical Review*, vol. 125, pp. 912–932, Feb. 1962. Publisher: American Physical Society.

[26] R. de Sousa and S. Das Sarma, "Theory of nuclear-induced spectral diffusion: Spin decoherence of phosphorus donors in Si and GaAs quantum dots," *Physical Review B*, vol. 68, p. 115322, Sept. 2003. Publisher: American Physical Society.

[27] W. M. Witzel and S. Das Sarma, "Quantum theory for electron spin decoherence induced by nuclear spin dynamics in semiconductor quantum computer architectures: Spectral diffusion of localized electron spins in the nuclear solid-state environment," *Phys. Rev. B*, vol. 74, p. 035322, Jul 2006.

[28] W. A. Coish and J. Baugh, "Nuclear spins in nanostructures," *physica status solidi (b)*, vol. 246, no. 10, pp. 2203–2215, 2009. _eprint: https://onlinelibrary.wiley.com/doi/pdf/10.1002/pssb.200945229.

[29] L. Cywiński, "Dephasing of electron spin qubits due to their interaction with nuclei in quantum dots," *Acta Physica Polonica A*, vol. 119, pp. 576–587, May 2011. arXiv:1009.4466 [cond-mat, physics:quant-ph].

[30] K. A. Al-Hassanieh, V. V. Dobrovitski, E. Dagotto, and B. N. Harmon, "Numerical modeling of the central spin problem using the spin-coherent-state p representation," *Phys. Rev. Lett.*, vol. 97, p. 037204, Jul 2006.

[31] O. Tsyplyatyev and D. Loss, "Spectrum of an Electron Spin Coupled to an Unpolarized Bath of Nuclear Spins," *Physical Review Letters*, vol. 106, p. 106803, Mar. 2011. Publisher: American Physical Society.

[32] N. A. Sinitsyn, Y. Li, S. A. Crooker, A. Saxena, and D. L. Smith, "Role of Nuclear Quadrupole Coupling on Decoherence and Relaxation of Central Spins in Quantum Dots," *Physical Review Letters*, vol. 109, p. 166605, Oct. 2012. Publisher: American Physical Society.

[33] C. L. Degen, F. Reinhard, and P. Cappellaro, "Quantum sensing," *Rev. Mod. Phys.*, vol. 89, p. 035002, Jul 2017.

[34] E. L. Hahn, "Spin Echoes," *Physical Review*, vol. 80, pp. 580–594, Nov. 1950. Publisher: American Physical Society.

[35] H. Y. Carr and E. M. Purcell, "Effects of Diffusion on Free Precession in Nuclear Magnetic Resonance Experiments," *Physical Review*, vol. 94, pp. 630–638, May 1954. Publisher: American Physical Society.

[36] L. Viola and S. Lloyd, "Dynamical suppression of decoherence in two-state quantum systems," *Physical Review A*, vol. 58, pp. 2733–2744, Oct. 1998. Publisher: American Physical Society.

[37] L. Cywiński, R. M. Lutchyn, C. P. Nave, and S. Das Sarma, "How to enhance dephasing time in superconducting qubits," *Phys. Rev. B*, vol. 77, p. 174509, May 2008.

[38] G. S. Uhrig, "Keeping a Quantum Bit Alive by Optimized $\ensuremath{\pi}$-Pulse Sequences," *Physical Review Letters*, vol. 98, p. 100504, Mar. 2007. Publisher: American Physical Society.

[39] E. A. Chekhovich, M. Hopkinson, M. S. Skolnick, and A. I. Tartakovskii, "Suppression of nuclear spin bath fluctuations in self-assembled quantum dots induced by inhomogeneous strain," *Nature Communications*, vol. 6, p. 6348, Feb. 2015. Publisher: Nature Publishing Group.

[40] A. Ajoy, U. Bissbort, D. Poletti, and P. Cappellaro, "Selective decoupling and hamiltonian engineering in dipolar spin networks," *Phys. Rev. Lett.*, vol. 122, p. 013205, Jan 2019.

[41] A. Imamoḡlu, E. Knill, L. Tian, and P. Zoller, "Optical pumping of quantum-dot nuclear spins," *Phys. Rev. Lett.*, vol. 91, p. 017402, Jul 2003.

[42] V. Jacques, P. Neumann, J. Beck, M. Markham, D. Twitchen, J. Meijer, F. Kaiser, G. Balasubramanian, F. Jelezko, and J. Wrachtrup, "Dynamic polarization of single nuclear spins by optical pumping of nitrogen-vacancy color centers in diamond at room temperature," *Phys. Rev. Lett.*, vol. 102, p. 057403, Feb 2009.

[43] A. Högele, M. Kroner, C. Latta, M. Claassen, I. Carusotto, C. Bulutay, and A. Imamoglu, "Dynamic nuclear spin polarization in the resonant laser excitation of an ingaas quantum dot," *Phys. Rev. Lett.*, vol. 108, p. 197403, May 2012.

[44] A. L. Falk, P. V. Klimov, V. Ivády, K. Szász, D. J. Christle, W. F. Koehl, A. Gali, and D. D. Awschalom, "Optical polarization of nuclear spins in silicon carbide," *Phys. Rev. Lett.*, vol. 114, p. 247603, Jun 2015.

[45] J. M. Taylor, C. M. Marcus, and M. D. Lukin, "Long-Lived Memory for Mesoscopic Quantum Bits," *Physical Review Letters*, vol. 90, p. 206803, May 2003. Publisher: American Physical Society.

[46] J. M. Taylor, A. Imamoglu, and M. D. Lukin, "Controlling a Mesoscopic Spin Environment by Quantum Bit Manipulation," *Physical Review Letters*, vol. 91, p. 246802, Dec. 2003. Publisher: American Physical Society.

[47] D. A. Gangloff, G. Éthier Majcher, C. Lang, E. V. Denning, J. H. Bodey, D. M. Jackson, E. Clarke, M. Hugues, C. Le Gall, and M. Atatüre, "Quantum interface of an electron and a nuclear ensemble," *Science*, vol. 364, pp. 62–66, Apr. 2019. Publisher: American Association for the Advancement of Science.

[48] E. V. Denning, D. A. Gangloff, M. Atatüre, J. Mørk, and C. Le Gall, "Collective Quantum Memory Activated by a Driven Central Spin," *Physical Review Letters*, vol. 123, p. 140502, Oct. 2019. Publisher: American Physical Society.

[49] M. V. G. Dutt, L. Childress, L. Jiang, E. Togan, J. Maze, F. Jelezko, A. S. Zibrov, P. R. Hemmer, and M. D. Lukin, "Quantum Register Based on Individual Electronic and Nuclear Spin Qubits in Diamond," *Science*, vol. 316, pp. 1312–1316, June 2007. Publisher: American Association for the Advancement of Science.

[50] P. Neumann, N. Mizuochi, F. Rempp, P. Hemmer, H. Watanabe, S. Yamasaki, V. Jacques, T. Gaebel, F. Jelezko, and J. Wrachtrup, "Multipartite Entanglement Among Single Spins in Diamond," *Science*, vol. 320, pp. 1326–1329, June 2008. Publisher: American Association for the Advancement of Science.

[51] G. D. Fuchs, G. Burkard, P. V. Klimov, and D. D. Awschalom, "A quantum memory intrinsic to single nitrogen–vacancy centres in diamond," *Nature Physics*, vol. 7, pp. 789–793, Oct. 2011. Publisher: Nature Publishing Group.

[52] T. H. Taminiau, J. Cramer, T. van der Sar, V. V. Dobrovitski, and R. Hanson, "Universal control and error correction in multi-qubit spin registers in diamond," *Nature Nanotechnology*, vol. 9, no. 3, pp. 171–176, 2014.

[53] L. Jiang, J. S. Hodges, J. R. Maze, P. Maurer, J. M. Taylor, D. G. Cory, P. R. Hemmer, R. L. Walsworth, A. Yacoby, A. S. Zibrov, and M. D. Lukin, "Repetitive readout of a single electronic spin via quantum logic with nuclear spin ancillae," *Science*, vol. 326, no. 5950, pp. 267–272, 2009.

[54] I. Lovchinsky, A. O. Sushkov, E. Urbach, N. P. de Leon, S. Choi, K. De Greve, R. Evans, R. Gertner, E. Bersin, C. Müller, L. McGuinness, F. Jelezko, R. L. Walsworth, H. Park, and M. D. Lukin, "Nuclear magnetic resonance detection and spectroscopy of single proteins using quantum logic," *Science*, vol. 351, pp. 836–841, Feb. 2016. Publisher: American Association for the Advancement of Science.

[55] P. Neumann, R. Kolesov, B. Naydenov, J. Beck, F. Rempp, M. Steiner, V. Jacques, G. Balasubramanian, M. L. Markham, D. J. Twitchen, S. Pezzagna, J. Meijer, J. Twamley, F. Jelezko, and J. Wrachtrup, "Quantum register based on coupled electron spins in a room-temperature solid," *Nature Physics*, vol. 6, pp. 249–253, Apr. 2010. Publisher: Nature Publishing Group.

[56] C. Bradley, J. Randall, M. Abobeih, R. Berrevoets, M. Degen, M. Bakker, M. Markham, D. Twitchen, and T. Taminiau, "A Ten-Qubit Solid-State Spin Register with Quantum Memory up to One Minute," *Physical Review X*, vol. 9, p. 031045, Sept. 2019. Publisher: American Physical Society.

[57] C. Bulutay, E. A. Chekhovich, and A. I. Tartakovskii, "Nuclear magnetic resonance inverse spectra of InGaAs quantum dots: Atomistic level structural information," *Physical Review B*, vol. 90, p. 205425, Nov. 2014. Publisher: American Physical Society.

[58] A. Ajoy, U. Bissbort, M. Lukin, R. Walsworth, and P. Cappellaro, "Atomic-Scale Nuclear Spin Imaging Using Quantum-Assisted Sensors in Diamond," *Physical Review X*, vol. 5, p. 011001, Jan. 2015. Publisher: American Physical Society.

[59] M. Kost, J. Cai, and M. B. Plenio, "Resolving single molecule structures with Nitrogen-vacancy centers in diamond," *Scientific Reports*, vol. 5, p. 11007, June 2015. Publisher: Nature Publishing Group.

[60] Z.-Y. Wang, J. F. Haase, J. Casanova, and M. B. Plenio, "Positioning nuclear spins in interacting clusters for quantum technologies and bioimaging," *Physical Review B*, vol. 93, p. 174104, May 2016. Publisher: American Physical Society.

[61] V. S. Perunicic, C. D. Hill, L. T. Hall, and L. C. L. Hollenberg, "A quantum spin-probe molecular microscope," *Nature Communications*, vol. 7, p. 12667, Oct. 2016. Publisher: Nature Publishing Group.

[62] J. Tang, Z. Yin, C. A. Hart, J. W. Blanchard, J. T. Oon, S. Bhalerao, J. M. Schloss, M. J. Turner, and R. L. Walsworth, "Quantum Diamond Microscope for Dynamic Imaging of Magnetic Fields," Sept. 2023. arXiv:2309.06587 [quant-ph] version: 1.

[63] J. R. Maze, P. L. Stanwix, J. S. Hodges, S. Hong, J. M. Taylor, P. Cappellaro, L. Jiang, M. V. G. Dutt, E. Togan, A. S. Zibrov, A. Yacoby, R. L. Walsworth, and M. D. Lukin, "Nanoscale magnetic sensing with an individual electronic spin in diamond," *Nature*, vol. 455, pp. 644–647, Oct. 2008. Publisher: Nature Publishing Group.

[64] C. A. Meriles, L. Jiang, G. Goldstein, J. S. Hodges, J. Maze, M. D. Lukin, and P. Cappellaro, "Imaging mesoscopic nuclear spin noise with a diamond magnetometer," *The Journal of Chemical Physics*, vol. 133, p. 124105, Sept. 2010.

[65] K. Arai, C. Belthangady, H. Zhang, N. Bar-Gill, S. J. DeVience, P. Cappellaro, A. Yacoby, and R. L. Walsworth, "Fourier magnetic imaging with nanoscale resolution and compressed sensing speed-up using electronic spins in diamond," *Nature Nanotechnology*, vol. 10, pp. 859–864, Oct. 2015. Publisher: Nature Publishing Group.

[66] M. H. Abobeih, J. Randall, C. E. Bradley, H. P. Bartling, M. A. Bakker, M. J. Degen, M. Markham, D. J. Twitchen, and T. H. Taminiau, "Atomic-scale imaging of a 27-nuclear-spin cluster using a quantum sensor," *Nature*, vol. 576, no. 7787, pp. 411–415, 2019.

[67] G. L. van de Stolpe, D. P. Kwiatkowski, C. E. Bradley, J. Randall, M. H. Abobeih, S. A. Breitweiser, L. C. Bassett, M. Markham, D. J. Twitchen, and T. H. Taminiau, "Mapping a 50-spin-qubit network through correlated sensing," *Nature Communications*, vol. 15, no. 1, p. 2006, 2024.

[68] W. Yao, R.-B. Liu, and L. J. Sham, "Theory of electron spin decoherence by interacting nuclear spins in a quantum dot," *Physical Review B*, vol. 74, p. 195301, Nov. 2006. Publisher: American Physical Society.

[69] R.-B. Liu, W. Yao, and L. J. Sham, "Control of electron spin decoherence caused by electron–nuclear spin dynamics in a quantum dot," *New Journal of Physics*, vol. 9, p. 226, July 2007.

[70] W. Yao, R.-B. Liu, and L. J. Sham, "Restoring Coherence Lost to a Slow Interacting Mesoscopic Spin Bath," *Physical Review Letters*, vol. 98, p. 077602, Feb. 2007. Publisher: American Physical Society.

[71] W. M. Witzel, R. de Sousa, and S. Das Sarma, "Quantum theory of spectral-diffusion-induced electron spin decoherence," *Phys. Rev. B*, vol. 72, p. 161306, Oct 2005.

[72] W. Yang and R.-B. Liu, "Quantum many-body theory of qubit decoherence in a finite-size spin bath," *Physical Review B*, vol. 78, p. 085315, Aug. 2008. Publisher: American Physical Society.

[73] W. Yang and R.-B. Liu, "Quantum many-body theory of qubit decoherence in a finite-size spin bath. II. Ensemble dynamics," *Physical Review B*, vol. 79, p. 115320, Mar. 2009. Publisher: American Physical Society.

[74] S. K. Saikin, W. Yao, and L. J. Sham, "Single-electron spin decoherence by nuclear spin bath: Linked-cluster expansion approach," *Physical Review B*, vol. 75, p. 125314, Mar. 2007. Publisher: American Physical Society.

[75] J. R. Maze, J. M. Taylor, and M. D. Lukin, "Electron spin decoherence of single nitrogen-vacancy defects in diamond," *Physical Review B*, vol. 78, p. 094303, Sept. 2008. Publisher: American Physical Society.

[76] L. T. Hall, J. H. Cole, and L. C. L. Hollenberg, "Analytic solutions to the central-spin problem for nitrogen-vacancy centers in diamond," *Physical Review B*, vol. 90, p. 075201, Aug. 2014. Publisher: American Physical Society.

[77] W. Yang, W.-L. Ma, and R.-B. Liu, "Quantum many-body theory for electron spin decoherence in nanoscale nuclear spin baths," *Reports on Progress in Physics*, vol. 80, p. 016001, nov 2016.

[78] D. Kwiatkowski and L. Cywiński, "Decoherence of two entangled spin qubits coupled to an interacting sparse nuclear spin bath: Application to nitrogen vacancy centers," *Physical Review B*, vol. 98, p. 155202, Oct. 2018. Publisher: American Physical Society.

[79] Z.-S. Yang, Y.-X. Wang, M.-J. Tao, W. Yang, M. Zhang, Q. Ai, and F.-G. Deng, "Longitudinal relaxation of a nitrogen-vacancy center in a spin bath by generalized cluster-correlation expansion method," *Annals of Physics*, vol. 413, p. 168063, 2020.

[80] M. Onizhuk, K. C. Miao, J. P. Blanton, H. Ma, C. P. Anderson, A. Bourassa, D. D. Awschalom, and G. Galli, "Probing the Coherence of Solid-State Qubits at Avoided Crossings," *PRX Quantum*, vol. 2, p. 010311, Jan. 2021. Publisher: American Physical Society.

[81] K. Ghosh, H. Ma, M. Onizhuk, V. Gavini, and G. Galli, "Spin–spin interactions in defects in solids from mixed all-electron and pseudopotential first-principles calculations," *npj Computational Materials*, vol. 7, pp. 1–8, July 2021. Publisher: Nature Publishing Group.

[82] M. Onizhuk, Y.-X. Wang, J. Nagura, A. A. Clerk, and G. Galli, "Understanding central spin decoherence due to interacting dissipative spin baths," *Phys. Rev. Lett.*, vol. 132, p. 250401, Jun 2024.

[83] N. B. Manson, M. Hedges, M. S. J. Barson, R. Ahlefeldt, M. W. Doherty, H. Abe, T. Ohshima, and M. J. Sellars, "Nv–n+ pair centre in 1b diamond," *New Journal of Physics*, vol. 20, p. 113037, nov 2018.

[84] M. W. Doherty, F. Dolde, H. Fedder, F. Jelezko, J. Wrachtrup, N. B. Manson, and L. C. L. Hollenberg, "Theory of the ground-state spin of the nv^- center in diamond," *Phys. Rev. B*, vol. 85, p. 205203, May 2012.

[85] G. Wolfowicz, F. J. Heremans, C. P. Anderson, S. Kanai, H. Seo, A. Gali, G. Galli, and D. D. Awschalom, "Quantum guidelines for solid-state spin defects," *Nature Reviews Materials*, vol. 6, no. 10, pp. 906–925, 2021.

[86] F. Casola, T. van der Sar, and A. Yacoby, "Probing condensed matter physics with magnetometry based on nitrogen-vacancy centres in diamond," *Nature Reviews Materials*, vol. 3, no. 1, p. 17088, 2018.

[87] G. Kucsko, P. C. Maurer, N. Y. Yao, M. Kubo, H. J. Noh, P. K. Lo, H. Park, and M. D. Lukin, "Nanometre-scale thermometry in a living cell," *Nature*, vol. 500, no. 7460, pp. 54–58, 2013.

[88] P. Neumann, I. Jakobi, F. Dolde, C. Burk, R. Reuter, G. Waldherr, J. Honert, T. Wolf, A. Brunner, J. H. Shim, D. Suter, H. Sumiya, J. Isoya, and J. Wrachtrup, "High-precision nanoscale temperature sensing using single defects in diamond," *Nano Letters*, vol. 13, pp. 2738–2742, 06 2013.

[89] M. S. J. Barson, P. Peddibhotla, P. Ovartchaiyapong, K. Ganesan, R. L. Taylor, M. Gebert, Z. Mielens, B. Koslowski, D. A. Simpson, L. P. McGuinness, J. McCallum, S. Prawer, S. Onoda, T. Ohshima, A. C. Bleszynski Jayich, F. Jelezko, N. B. Manson, and M. W. Doherty, "Nanomechanical sensing using spins in diamond," *Nano Letters*, vol. 17, pp. 1496–1503, 03 2017.

[90] M. P. Ledbetter, K. Jensen, R. Fischer, A. Jarmola, and D. Budker, "Gyroscopes based on nitrogen-vacancy centers in diamond," *Phys. Rev. A*, vol. 86, p. 052116, Nov 2012.

[91] J. M. Taylor, P. Cappellaro, L. Childress, L. Jiang, D. Budker, P. R. Hemmer, A. Yacoby, R. Walsworth, and M. D. Lukin, "High-sensitivity diamond magnetometer with nanoscale resolution," *Nature Physics*, vol. 4, no. 10, pp. 810–816, 2008.

[92] F. Dolde, H. Fedder, M. W. Doherty, T. Nöbauer, F. Rempp, G. Balasubramanian, T. Wolf, F. Reinhard, L. C. L. Hollenberg, F. Jelezko, and J. Wrachtrup, "Electric-field sensing using single diamond spins," *Nature Physics*, vol. 7, no. 6, pp. 459–463, 2011.

[93] C. Li, R. Soleyman, M. Kohandel, and P. Cappellaro, "Sars-cov-2 quantum sensor based on nitrogen-vacancy centers in diamond," *Nano Letters*, vol. 22, pp. 43–49, 01 2022.

[94] N. Aslam, H. Zhou, E. K. Urbach, M. J. Turner, R. L. Walsworth, M. D. Lukin, and H. Park, "Quantum sensors for biomedical applications," *Nature Reviews Physics*, vol. 5, no. 3, pp. 157–169, 2023.

[95] D. Braun, G. Adesso, F. Benatti, R. Floreanini, U. Marzolino, M. W. Mitchell, and S. Pirandola, "Quantum-enhanced measurements without entanglement," *Rev. Mod. Phys.*, vol. 90, p. 035006, Sep 2018.

[96] V. Giovannetti, S. Lloyd, and L. Maccone, "Quantum-enhanced measurements: Beating the standard quantum limit," *Science*, vol. 306, no. 5700, pp. 1330–1336, 2004.

[97] J. M. E. Fraisse and D. Braun, "Coherent averaging," *Ann. Phys.*, vol. 527, no. 9-10, pp. 701–712, 2015.

[98] W. Zheng, K. Bian, X. Chen, Y. Shen, S. Zhang, R. Stöhr, A. Denisenko, J. Wrachtrup, S. Yang, and Y. Jiang, "Coherence enhancement of solid-state qubits by local manipulation of the electron spin bath," *Nature Physics*, vol. 18, no. 11, pp. 1317–1323, 2022.

[99] M. Steiner, P. Neumann, J. Beck, F. Jelezko, and J. Wrachtrup, "Universal enhancement of the optical readout fidelity of single electron spins at nitrogen-vacancy centers in diamond," *Phys. Rev. B*, vol. 81, p. 035205, Jan 2010.

[100] D. Le Sage, L. M. Pham, N. Bar-Gill, C. Belthangady, M. D. Lukin, A. Yacoby, and R. L. Walsworth, "Efficient photon detection from color centers in a diamond optical waveguide," *Phys. Rev. B*, vol. 85, p. 121202(R), Mar 2012.

[101] D. A. Hopper, R. R. Grote, S. M. Parks, and L. C. Bassett, "Amplified sensitivity of nitrogen-vacancy spins in nanodiamonds using all-optical charge readout," *ACS Nano*, vol. 12, pp. 4678–4686, 05 2018.

[102] J.-C. Jaskula, B. J. Shields, E. Bauch, M. D. Lukin, A. S. Trifonov, and R. L. Walsworth, "Improved quantum sensing with a single solid-state spin via spin-to-charge conversion," *Phys. Rev. Appl.*, vol. 11, p. 064003, Jun 2019.

[103] L. Orphal-Kobin, K. Unterguggenberger, T. Pregnolato, N. Kemf, M. Matalla, R.-S. Unger, I. Ostermay, G. Pieplow, and T. Schröder, "Optically coherent nitrogen-vacancy defect centers in diamond nanostructures," *Phys. Rev. X*, vol. 13, p. 011042, Mar 2023.

[104] O. Sahin, E. de Leon Sanchez, S. Conti, A. Akkiraju, P. Reshetikhin, E. Druga, A. Aggarwal, B. Gilbert, S. Bhave, and A. Ajoy, "High field magnetometry with hyperpolarized nuclear spins," *Nature Communications*, vol. 13, no. 1, p. 5486, 2022.

[105] H. J. Mamin, M. H. Sherwood, M. Kim, C. T. Rettner, K. Ohno, D. D. Awschalom, and D. Rugar, "Multipulse double-quantum magnetometry with near-surface nitrogen-vacancy centers," *Phys. Rev. Lett.*, vol. 113, p. 030803, Jul 2014.

[106] A. Jarmola, S. Lourette, V. M. Acosta, A. G. Birdwell, P. Blümler, D. Budker, T. Ivanov, and V. S. Malinovsky, "Demonstration of diamond nuclear spin gyroscope," *Science Advances*, vol. 7, no. 43, p. eabl3840, 2021.

[107] J. Rovny, Z. Yuan, M. Fitzpatrick, A. I. Abdalla, L. Futamura, C. Fox, M. C. Cambria, S. Kolkowitz, and N. P. de Leon, "Nanoscale covariance magnetometry with diamond quantum sensors," *Science*, vol. 378, no. 6626, pp. 1301–1305, 2022.

[108] P. Wang, W. Yang, and R. Liu, "Using weak measurements to synthesize projective measurement of nonconserved observables of weakly coupled nuclear spins," *Phys. Rev. Appl.*, vol. 19, p. 054037, May 2023.

[109] L. Gassab and Ö. E. Müstecaplıoğlu, "Spin Squeezing Enhanced Quantum Magnetometry with Nitrogen-Vacancy Center Qutrits," June 2024. arXiv:2406.15324 [quant-ph].

[110] N. M. Nusran, M. U. Momeen, and M. V. G. Dutt, "High-dynamic-range magnetometry with a single electronic spin in diamond," *Nature Nanotechnology*, vol. 7, no. 2, pp. 109–113, 2012.

[111] H. T. Dinani, D. W. Berry, R. Gonzalez, J. R. Maze, and C. Bonato, "Bayesian estimation for quantum sensing in the absence of single-shot detection," *Phys. Rev. B*, vol. 99, p. 125413, Mar 2019.

[112] I. Zohar, B. Haylock, Y. Romach, M. J. Arshad, N. Halay, N. Drucker, R. Stöhr, A. Denisenko, Y. Cohen, C. Bonato, and A. Finkler, "Real-time frequency estimation of a qubit without single-shot-readout," *Quantum Science and Technology*, vol. 8, p. 035017, may 2023.

[113] A. Gupta, L. Hacquebard, and L. Childress, "Efficient signal processing for time-resolved fluorescence detection of nitrogen-vacancy spins in diamond," *J. Opt. Soc. Am. B*, vol. 33, pp. B28–B34, Mar 2016.

[114] N. Xu, F. Zhou, X. Ye, X. Lin, B. Chen, T. Zhang, F. Yue, B. Chen, Y. Wang, and J. Du, "Noise prediction and reduction of single electron spin by deep-learning-enhanced feedforward control," *Nano Letters*, vol. 23, pp. 2460–2466, 04 2023.

[115] I. Daubechies, J. Lu, and H.-T. Wu, "Synchrosqueezed wavelet transforms: An empirical mode decomposition-like tool," *Applied and Computational Harmonic Analysis*, vol. 30, no. 2, pp. 243–261, 2011.

[116] C. S. Burrus, R. A. Gopinath, and H. Guo, *Introduction to wavelets and wavelet transforms: a primer*. Upper Saddle River, N.J: Prentice Hall, 1998.

[117] P. S. Addison, *The Illustrated Wavelet Transform Handbook: Introductory Theory and Applications in Science, Engineering, Medicine and Finance*. Boca Raton: CRC Press, 2017.

[118] B. P. Abbott *et al.*, "Observation of gravitational waves from a binary black hole merger," *Phys. Rev. Lett.*, vol. 116, p. 061102, Feb 2016.

[119] N. Xu, F. Jiang, Y. Tian, J. Ye, F. Shi, H. Lv, Y. Wang, J. Wrachtrup, and J. Du, "Wavelet-based fast time-resolved magnetic sensing with electronic spins in diamond," *Phys. Rev. B*, vol. 93, p. 161117(R), Apr 2016.

[120] A. E. Seedhouse, N. D. Stuyck, S. Serrano, T. Tanttu, W. Gilbert, J. Y. Huang, F. E. Hudson, K. M. Itoh, A. Laucht, W. H. Lim, *et al.*,

"Spatio-temporal correlations of noise in mos spin qubits," *arXiv preprint arXiv:2309.12542*, 2023.

[121] "2024 Tour de France: Results from Stage 21," July 2024. Section: Tour de France.

[122] P. Goupillaud, A. Grossmann, and J. Morlet, "Cycle-octave and related transforms in seismic signal analysis," *Geoexploration*, vol. 23, no. 1, pp. 85–102, 1984. Seismic Signal Analysis and Discrimination III.

[123] G. Yu, "A multisynchrosqueezing-based high-resolution time-frequency analysis tool for the analysis of non-stationary signals," *Journal of Sound and Vibration*, vol. 492, p. 115813, 2021.

[124] I. Daubechies, *Ten Lectures on Wavelets*. Society for Industrial and Applied Mathematics, 1992.

[125] S. Mallat, "A theory for multiresolution signal decomposition: the wavelet representation," *IEEE Transactions on Pattern Analysis and Machine Intelligence*, vol. 11, no. 7, pp. 674–693, 1989.

[126] M. Stéphane, "Chapter 7 - wavelet bases," in *A Wavelet Tour of Signal Processing (Third Edition)* (M. Stéphane, ed.), pp. 263–376, Boston: Academic Press, third edition ed., 2009.

[127] D. L. Donoho and I. M. Johnstone, "Ideal spatial adaptation by wavelet shrinkage," *Biometrika*, vol. 81, pp. 425–455, 09 1994.

[128] D. L. Donoho, I. M. Johnstone, G. Kerkyacharian, and D. Picard, "Wavelet shrinkage: Asymptopia?," *Journal of the Royal Statistical Society: Series B (Methodological)*, vol. 57, no. 2, pp. 301–337, 1995.

[129] D. L. Donoho and I. M. Johnstone, "Minimax estimation via wavelet shrinkage," *The Annals of Statistics*, vol. 26, no. 3, pp. 879 – 921, 1998.

[130] L. Breiman, "Better subset regression using the nonnegative garrote," *Technometrics*, vol. 37, no. 4, pp. 373–384, 1995.

[131] E. T. Güldeste and C. Bulutay, "Wavelet resolved coherence beating in the overhauser field of a thermal nuclear spin ensemble," *Phys. Rev. B*, vol. 105, p. 075202, Feb 2022.

[132] W. M. Witzel and S. Das Sarma, "Wavefunction considerations for the central spin decoherence problem in a nuclear spin bath," *Phys. Rev. B*, vol. 77, p. 165319, Apr 2008.

[133] G. Giedke, J. M. Taylor, D. D'Alessandro, M. D. Lukin, and A. Imamoğlu, "Quantum measurement of a mesoscopic spin ensemble," *Phys. Rev. A*, vol. 74, p. 032316, Sep 2006.

[134] A. Abragam, *The principles of nuclear magnetism*. Oxford University Press, 1961.

[135] C. P. Slichter, *Principles of magnetic resonance*. Springer Berlin Heidelberg, 1990.

[136] L. Cywiński, W. M. Witzel, and S. Das Sarma, "Pure quantum dephasing of a solid-state electron spin qubit in a large nuclear spin bath coupled by long-range hyperfine-mediated interactions," *Phys. Rev. B*, vol. 79, p. 245314, Jun 2009.

[137] W.-L. Ma, G. Wolfowicz, S.-S. Li, J. J. L. Morton, and R.-B. Liu, "Classical nature of nuclear spin noise near clock transitions of bi donors in silicon," *Phys. Rev. B*, vol. 92, p. 161403, Oct 2015.

[138] J. Schliemann, A. Khaetskii, and D. Loss, "Electron spin dynamics in quantum dots and related nanostructures due to hyperfine interaction with nuclei," *Journal of Physics: Condensed Matter*, vol. 15, p. R1809, dec 2003.

[139] E. T. Güldeste and C. Bulutay, "Loschmidt echo driven by hyperfine and electric-quadrupole interactions in nanoscale nuclear spin baths," *Phys. Rev. B*, vol. 98, p. 085202, Aug 2018.

[140] R. Giri, C. Dorigoni, S. Tambalo, F. Gorrini, and A. Bifone, "Selective measurement of charge dynamics in an ensemble of nitrogen-vacancy centers

in nanodiamond and bulk diamond," *Phys. Rev. B*, vol. 99, p. 155426, Apr 2019.

[141] S. Meignen, T. Oberlin, and S. McLaughlin, "A new algorithm for multicomponent signals analysis based on synchrosqueezing: With an application to signal sampling and denoising," *IEEE Transactions on Signal Processing*, vol. 60, no. 11, pp. 5787–5798, 2012.

[142] W. M. Witzel, M. S. Carroll, L. Cywiński, and S. Das Sarma, "Quantum decoherence of the central spin in a sparse system of dipolar coupled spins," *Phys. Rev. B*, vol. 86, p. 035452, Jul 2012.

[143] C. Bulutay, "Quadrupolar spectra of nuclear spins in strained $in_xga_{1-x}as$ quantum dots," *Phys. Rev. B*, vol. 85, p. 115313, Mar 2012.

[144] P. Szańkowski, G. Ramon, J. Krzywda, D. Kwiatkowski, and L. Cywiński, "Environmental noise spectroscopy with qubits subjected to dynamical decoupling," *Journal of Physics: Condensed Matter*, vol. 29, p. 333001, jul 2017.

[145] G. Ramon, "Non-gaussian signatures and collective effects in charge noise affecting a dynamically decoupled qubit," *Phys. Rev. B*, vol. 92, p. 155422, Oct 2015.

[146] "Nautical Vintage 3" - Antique Style Brass Directional Pocket Compass."

[147] M. W. Doherty, N. B. Manson, P. Delaney, F. Jelezko, J. Wrachtrup, and L. C. Hollenberg, "The nitrogen-vacancy colour centre in diamond," *Physics Reports*, vol. 528, no. 1, pp. 1–45, 2013. The nitrogen-vacancy colour centre in diamond.

[148] J. R. Maze, A. Dréau, V. Waselowski, H. Duarte, J.-F. Roch, and V. Jacques, "Free induction decay of single spins in diamond," *New Journal of Physics*, vol. 14, p. 103041, oct 2012.

[149] N. Zhao, S.-W. Ho, and R.-B. Liu, "Decoherence and dynamical decoupling control of nitrogen vacancy center electron spins in nuclear spin baths," *Phys. Rev. B*, vol. 85, p. 115303, Mar 2012.

[150] E. T. Güldeste and C. Bulutay, "Wavelet-based ramsey magnetometry enhancement of a single nv center in diamond," 2024.

[151] B. J. Shields, Q. P. Unterreithmeier, N. P. de Leon, H. Park, and M. D. Lukin, "Efficient readout of a single spin state in diamond via spin-to-charge conversion," *Phys. Rev. Lett.*, vol. 114, p. 136402, Mar 2015.

[152] J. T. Oon, J. Tang, C. A. Hart, K. S. Olsson, M. J. Turner, J. M. Schloss, and R. L. Walsworth, "Ramsey envelope modulation in nv diamond magnetometry," *Phys. Rev. B*, vol. 106, p. 054110, Aug 2022.

[153] G. P. Nason, ed., *Wavelet Shrinkage*, pp. 83–132. New York, NY: Springer New York, 2008.

[154] S. M. Kay, *Fundamentals of Statistical Signal Processing: Estimation Theory*. Englewood Cliffs, NJ: Prentice Hall, 1993.

[155] G. Casella and R. L. Berger, *Statistical Inference*. Pacific Grove, CA: Duxbury Press, second ed., 2002.

[156] T. Ishikawa, K.-M. C. Fu, C. Santori, V. M. Acosta, R. G. Beausoleil, H. Watanabe, S. Shikata, and K. M. Itoh, "Optical and spin coherence properties of nitrogen-vacancy centers placed in a 100 nm thick isotopically purified diamond layer," *Nano Letters*, vol. 12, pp. 2083–2087, 04 2012.

[157] "F1 - The Official Home of Formula 1® Racing," Feb. 2024.

[158] "IRONMAN 70.3 100+ photos: Taking it to the limit in Hobart."